LAWRENCE
LIVERMORE
NATIONAL
LABORATORY

LLNL-TR-679938

FY15 LLNL OMEGA Experimental Programs

R. F. Heeter, K. L. Baker, M. A. Barrios, M. A. Beckwith, D. T. Casey, P. M. Celliers, H. Chen, F. Coppari, K. B. Fournier, D. E. Fratanduono, J. Frenje, C. M. Huntington, R. G. Kraus, A. E. Lazicki, D. A. Martinez, J. M. McNaney, M. A. Millot, A. E. Pak, H. S. Park, Y. Ping, B. B. Pollock, R. F. Smith, C. E. Wehrenberg, K. Widmann, G. W. Collins, O. L. Landen, A. Wan, W. Hsing

December 4, 2015

Disclaimer

This work performed under the auspices of the U.S. Department of Energy by Lawrence Livermore National Laboratory under Contract DE-AC52-07NA27344.

FY15 LLNL OMEGA Experimental Programs

R.F. Heeter, K.L. Baker, M.A. Barrios, M.A. Beckwith, D.T. Casey, P.M. Celliers, H. Chen, F. Coppari, K.B. Fournier, D.E. Fratanduono, J. Frenje (MIT), C.M. Huntington, R.G. Kraus, A.E. Lazicki, D.A. Martinez, J.M. McNaney, M.A. Millot, A.E. Pak, H.-S. Park, Y. Ping, B.B. Pollock, R.F. Smith, C.E. Wehrenberg, K. Widmann, G.W. Collins, O.L. Landen, A. Wan, and W. Hsing

In FY15, LLNL's High-Energy-Density Physics (HED) and Indirect Drive Inertial Confinement Fusion (ICF-ID) programs conducted several campaigns on the OMEGA laser system and on the EP laser system, as well as campaigns that used the OMEGA and EP beams jointly. Overall these LLNL programs led 468 target shots in FY15, with 315 shots using just the OMEGA laser system, 145 shots using just the EP laser system, and 8 Joint shots using Omega and EP together. Approximately 25% of the total number of shots (56 OMEGA shots and 67 EP shots, including the 8 Joint shots) supported the Indirect Drive Inertial Confinement Fusion Campaign (ICF-ID). The remaining 75% (267 OMEGA shots and 86 EP shots) were dedicated to experiments for High-Energy-Density Physics (HED). Highlights of the various HED and ICF campaigns are summarized in the following reports.

In addition to these experiments, LLNL Principal Investigators led a variety of Laboratory Basic Science campaigns using OMEGA and EP, including 90 target shots using just OMEGA and 61 shots using just EP. The highlights of these are also summarized, following the ICF and HED campaigns.

In total, LLNL led a total of 619 shots at LLE in FY 2015. In addition, LLNL PIs also supported 39 NLUF shots on Omega and 35 NLUF shots on EP, in collaboration with the academic community.

This work performed under the auspices of the U.S. Department of Energy by Lawrence Livermore National Laboratory under Contract DE-AC52-07NA27344.

Table of Contents

Indirect Drive Inertial Confinement Fusion Experiments

1. Diamond Sound Speed Measurements Along the Principal Hugoniot (PI: D.E. Fratanduono)

Sound speed measurements along the principal Hugoniot of ablator materials are an important constraint in ICF experiments, since the sound speed in the ablator influences the instability growth rate. Accurate sound speed measurements of diamond in this regime would further develop this ablator material, and aid our understanding of the ICF instability growth rates. In this campaign, the diamond sound speed was measured using a recently developed perturbation analysis.[1] Specially designed pulse shapes were used on two half-days of Omega shots to create a rippled ablation drive. For a monolithic target, the correlation between ripples in the drive and at the shock front can be used to determine the sample sound speed. For the first half day of experiments, diamond blanking was an issue, and no usable data was obtained. For the second half-day, two target designs were fielded. A new design with a preheat shield was used, but the delivered laser energy was too low to produce a reflective shock in diamond. The second target design utilized a two-section target in which perturbations were tracked in both the diamond sample and a quartz witness. By correlating the perturbations in each material, and with the assumption the quartz EOS is known, the diamond sound speed was determined. This alternative design produced excellent experimental data. It was found that these measurements are in good agreement with the preferred EOS table (LEOS 9061) use in ICF simulations.

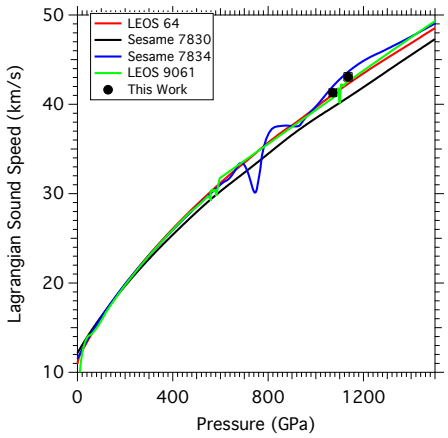

Figure 1: Diamond sound speed measurements compared with EOS models

[1] Fratanduono, D. E., D. H. Munro, P. M. Celliers and G. W. Collins (2014). "Hugoniot experiments with unsteady waves." Journal of Applied Physics **116**(3): 033517.

2. Mix Effects in Tungsten-Doped Be Capsules Probed with Omega-EP Short Pulse Radiography (PI: D.T. Casey)

An OMEGA/EP Joint shot day was dedicated to following up on results from ablator physics measurements using beryllium capsules in FY13. The prior campaign was useful in assessing the performance of Be as an ablator for indirect drive ignition experiments on the NIF, and also proved to be an interesting mix experiment.[1] The second round of experiments in FY15 used Be capsules driven by gold hohlraums (1.6 mm diameter by 2.1 mm long by 50 μm thick) that were irradiated by 40 OMEGA laser beams. The shots were diagnosed with the OMEGA neutronics suite and also radiography using EP driven, copper K-alpha backlighting, observed with the spherical crystal imager. The spherical crystal imager gave high quality radiographs both time gated and time integrated. The time gated images were taken to remove capsule self emission, but had reduced photon statistics compared to the time integrated image plates.

The capsules were 40 um thick Be shells, 610 μm in diameter, with the inner 14 μm of Be also doped with 4% Cu. They were filled with deuterium gas. Several targets also included thin 0.5 μm tungsten (W) layers, either on the inner capsule surface or recessed 5 μm to provide radiographic contrast to test mix models. Figure 2 below shows the radiograph geometry, a sample EP backlight radiograph with the spherical crystal imager, and a time integrated self emission image. The X-ray self emission images show unexpected strong 3D asymmetry.

Three types of capsules were shot, as shown schematically in Figure 3. Figure 3 also summarizes the yield and T_{ion} observed with the neutronics suite. The yield behavior is interesting, showing larger variability than in 2013, both with and without W. Surprisingly, the buried-W data shows lower yields than W at gas/shell interface. Detailed comparisons with simulations are now underway.

[1]D. T. Casey et al., PRL 114, 205002 (2015).

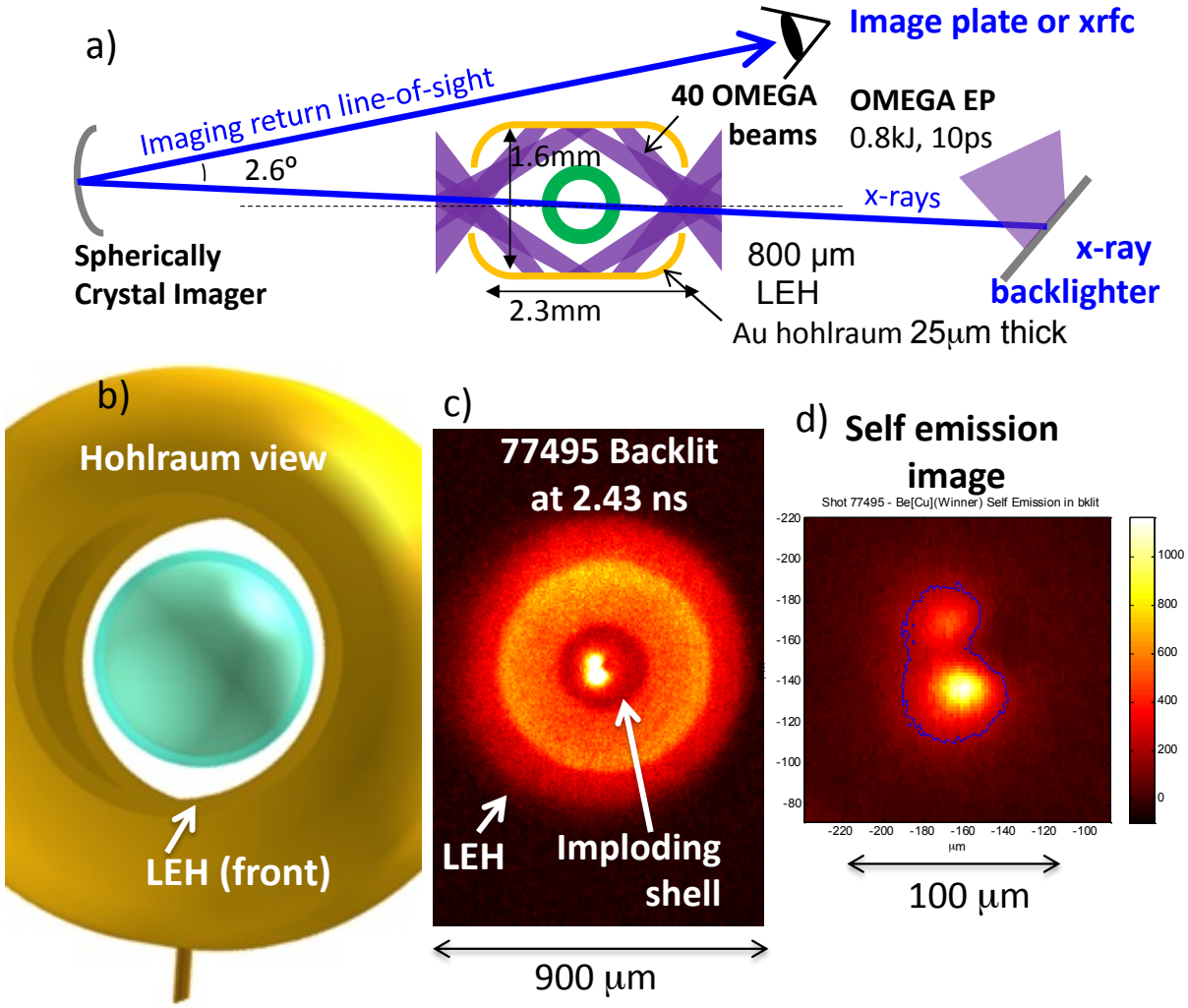

Figure 1: a) Experimental schematic showing the EP backlighting geometry using the spherical crystal imager. b) Rendering of the spherical crystal imager's view down the hohlraum axis. c) Backlit image of the shell in flight at 2.43 ns. d) Time integrated self-emission image of hotspot, showing strong asymmetry.

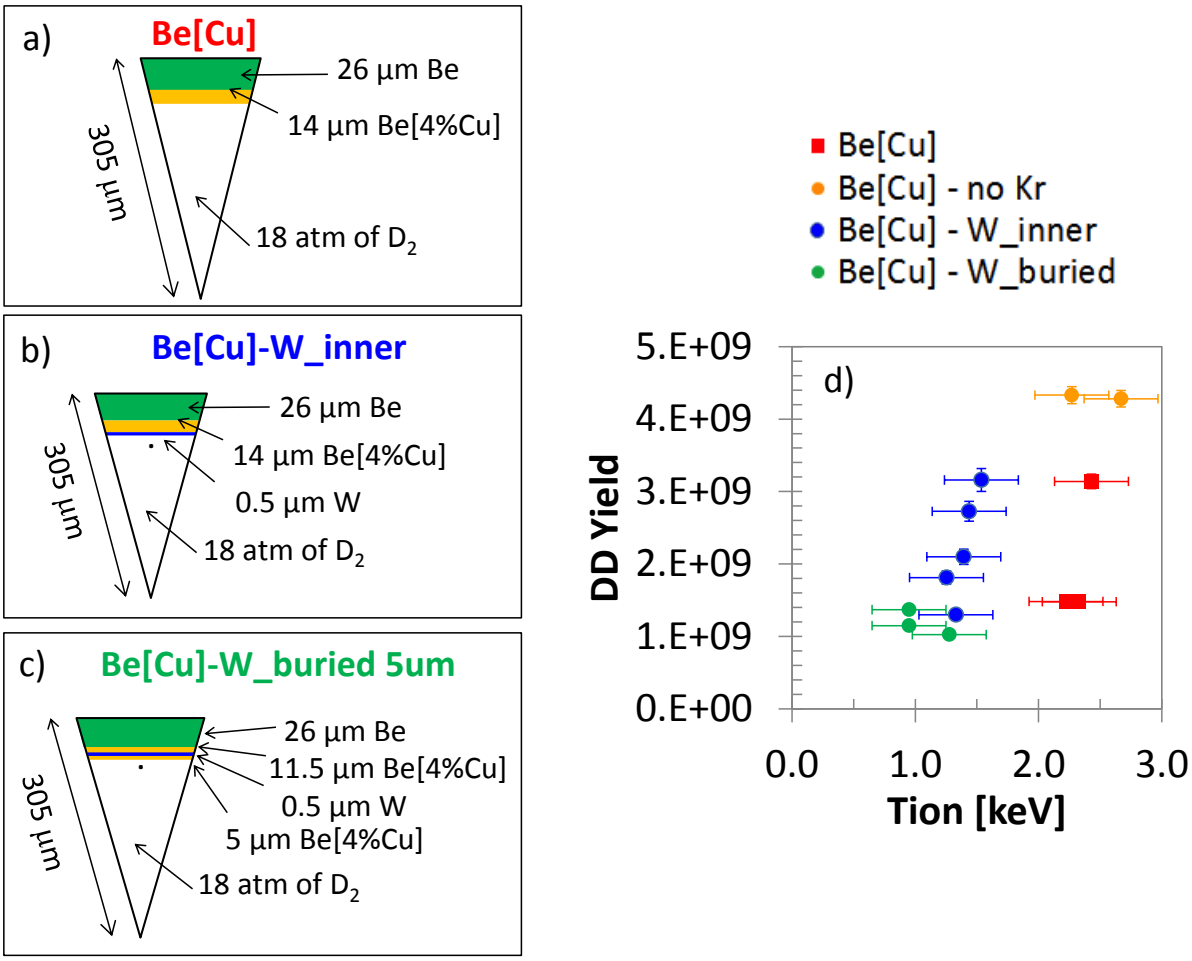

Figure 2: a) Cu doped Be capsule schematic. b) Cu doped Be capsule schematic with a 0.5um W layer at the gas/shell interface. c) Cu doped Be capsule schematic with a 0.5um W layer recessed 5um from the gas/shell interface. d) Summary of the DD neutron yield and measured Tion for each configuration.

3. Hohlraum Drive Measurements Using a Shock Witness Plate (PI: K.L Baker)

With designers S. MacLaren and R. Olson

The purpose of this Omega half-day campaign was to measure the temporal and spatial profile of the drive in a hohlraum using a VISAR package on the side of the hohlraum, and then to assess whether this technique could be used to directly detect laser beams hitting the wall of the hohlraum. Such a method can be used to evaluate cross-beam energy transfer. As shown in Figure 1, these experiments used a two shock laser pulse, SS1503vA01**,** hitting a vacuum gold hohlraum oriented along the P6/P7 axis with a gold M-band block/ablator material placed on a quartz window in one part of the hohlraum wall. This campaign set the stage for similar, subsequent NIF VISAR shots, which have shown that the gold M-band block can itself result in multiple shocks not predicted in simulations, perhaps due to the gold/quartz rarefaction wave interacting with the ablation front, so a future campaign would preferably use an aluminum ablator. On these Omega shots a 2.5 mm VISAR cone partly protected the window from unconverted light; however, due to the potentially large level entering the chamber (up to 4%), a much longer VISAR cone (>8 mm), would be recommended on future campaigns.

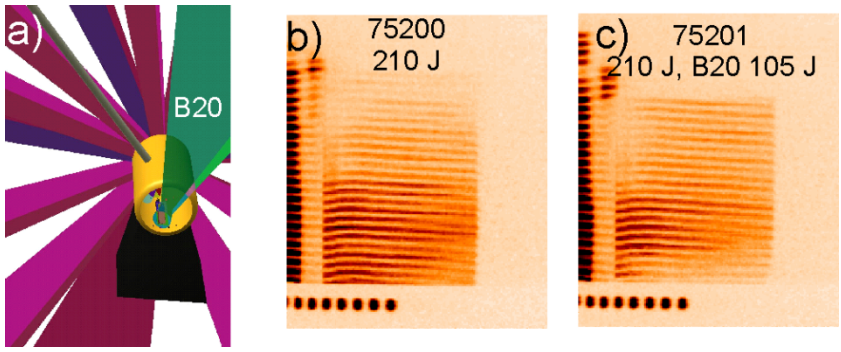

Figure 1: (a) VisRad image of the hohlraum with beam 20 directly hitting the ablator located on the VISAR window. (b) VISAR measurement of the drive with beam 20 not hitting the VISAR window and (c). VISAR measurement of the drive with beam 20 hitting the VISAR window.

4. Fast X-ray Imaging Using Optical Interferometry (PI: K.L. Baker)

with P. Celliers and M. Tabak

The purpose of this campaign was to demonstrate high spatial and temporal resolution x-ray imaging using the optical VISAR and OHRV diagnostics. This approach utilized a semiconductor, with the side facing the backlighter capsule coated with a thin aluminum relecting layer. X-rays passing through the metal layer and get absorbed in the semiconductor, changing the index of refraction. The other side of the semiconductor was AR coated, to allow the VISAR or OHRV probe beam to probe the phase of the semiconductor as the x-rays were absorbed in the semiconductor. This technique is capable of acquiring sub-picosecond 2-D or 1-D x-ray images with detector spatial resolution of better than 10 um, and offers the ability to operate in the high neutron flux environment expected on ignition shots with burning plasmas. This experiment used 39 beams of the OMEGA laser to implode a backlighter capsule, 890 um diameter and 9 um thick, with a 1 ns pulse length. The x-ray emission was then imaged onto a semiconductor, diamond or quartz, using a miniature x-ray snout as shown in Fig. 1a. As displayed in Fig. 1b, the VISAR then probed the semiconductor from the back and measured the induced phase change inside the semiconductor due to the impinging x-rays. A lineout of the semiconductor phase change measured by the VISAR is then compared to channel 11 of the (slower) DANTE x-ray diode array, in Fig. 1c.

.

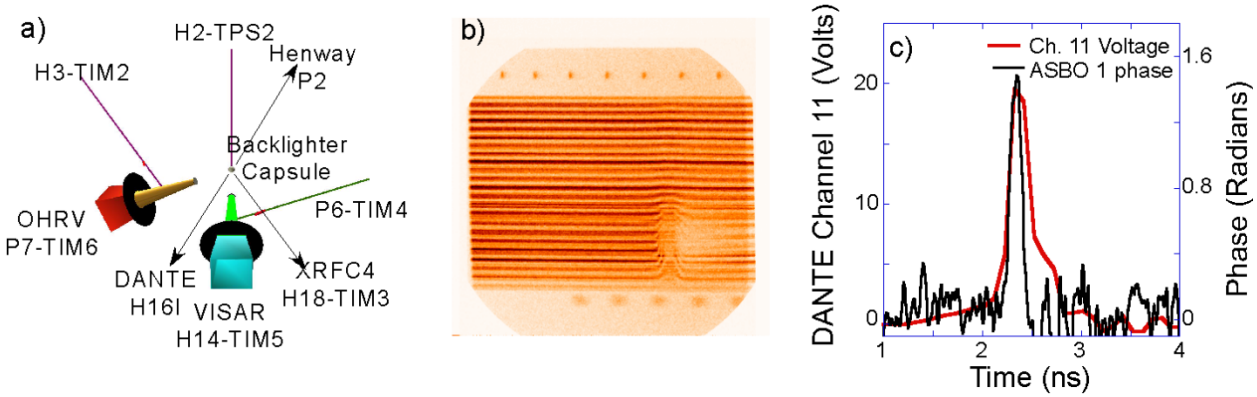

Figure 1: (a) VisRad image of the experimental setup to image the backlighter capsule onto a semiconductor. (b) VISAR measurement of the x-ray induced phase change in the semiconductor and (c). Lineout comparison of the DANTE channel 11 trace(red) with the VISAR trace(black).

5. Rayleigh-Taylor Growth Measurements on Aluminum Ablators (PI: D.T. Casey)

Aluminum has attractive properties as a potential ICF ablator, including the ability to shield Au hohlraum M-band without dopants via its mid-Z opacity, being a single species material, and having a well-understood equation of state. On the other hand, the presumptive low ablation velocity and high opacity may make it more unstable to the Rayleigh-Taylor (RT) instability compared to other ablators such as Be, HDC, and CH. However, some predictions suggest a double ablation front may form (thermal and M-band) which may decrease RT growth by increasing the ablative stabilization through a larger effective density scale length. This Joint shot day sought to test RT growth rates in Al using face on radiography and to develop a platform for testing the possible impact of a double ablation front feature. This work complemented a LANL experiment conducted the same week to measure the mass ablation rate of Al. Aluminum RT growth data were obtained that will be compared to calculations. Progress was slowed by anomalously-early Au-halfraum closure obscuring the backlighter, which limited the number of drives that could be tested, but enough data were obtained to do initial comparisons to simulation. Figure 1 shows the halfraum-and-sidelighter configuration used to constrain the trajectory of the Al package. Figure 2 shows the face-on RT data obtained at 3.7 ns.

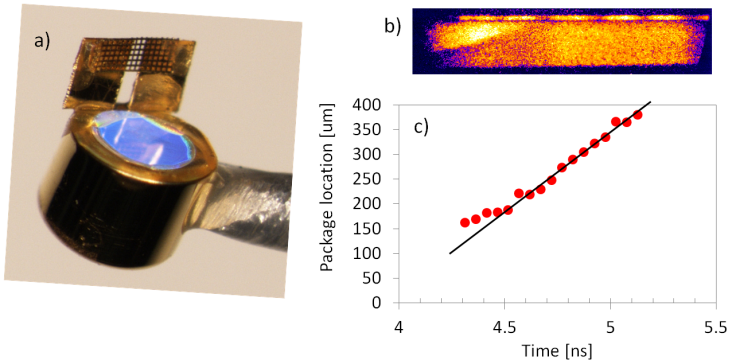

Figure 1: a) Sidelighter halfraum to measure trajectory of Al package. b) Raw streak camera radiograph of sidelit Al package. c) Measured Al package trajectory, which will provide a good constraint on Al ablation properties and hohlraum drive.

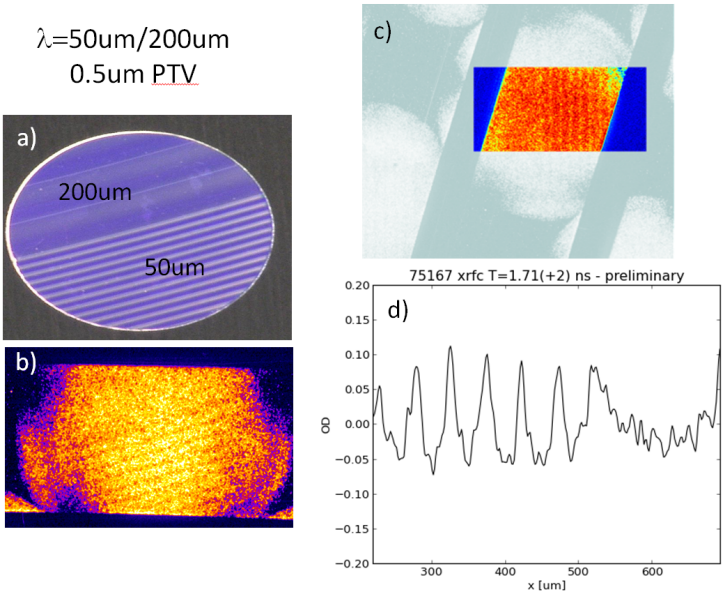

Figure 2: a) Al RT package with 200um and 50um sinusoidal modulations. c) Raw X-ray framing camera radiograph of Al RT package at 3.7ns. c) Orientation of lineout for optical depth analysis. d) Optical depth lineout from region shown in part c, showing good observed modulation growth.

6. Hohlraum Magnetization Using Laser-Driven Currents (PI: B.B. Pollock)

with J. Moody, J.S. Ross, D. Turnbull, C. Goyon, A. Hazi, G. Swadling and W. Farmer

In FY15 the Hohlraum Faraday Rotation campaigns continued with 2 days on Omega EP. This continued the investigation of the feasibility of self-magnetizing hohlraum targets for ICF applications. The basic target design consists of a half-loop formed by folding a thin gold sheet around a 500 um diameter fused Si rod. On the open side of the loop are parallel plates, into one of which holes were placed so that the EP long pulse beams could shine through to produce a plasma at the surface of the second plate, as shown in Figure X. Hot electrons formed at this plasma collect around the holes in the first plate, essentially charging up a parallel plate capacitor. The half-loop connects the plates, allowing current to flow and produce a magnetic field on the loop axis. The first FY15 campaign studied variations on this approach by changing the longitudinal structure of the loop portion of the target and by expanding the loop diameter. The EP 4w probe capability was employed to directly measure the magnetic field inside the loop via Faraday rotation along the hohlraum axis. Fields up to 4.6 T were measured at the time of the probe beam. In the second shot day, the short-pulse backlighter beam was used to drive a proton source for proton deflectometry measurements of the fringing magnetic fields around the target. This campaign allowed additional parameter scans and extended the previous data set. This shot day included collaborators from ILE (Osaka University) who have performed initial analysis on the proton data, which indicate magnetic fields of ~70 T can be produced in the standard target geometry. The analysis of this recent experiment is ongoing and will inform the FY16 continuation of this effort.

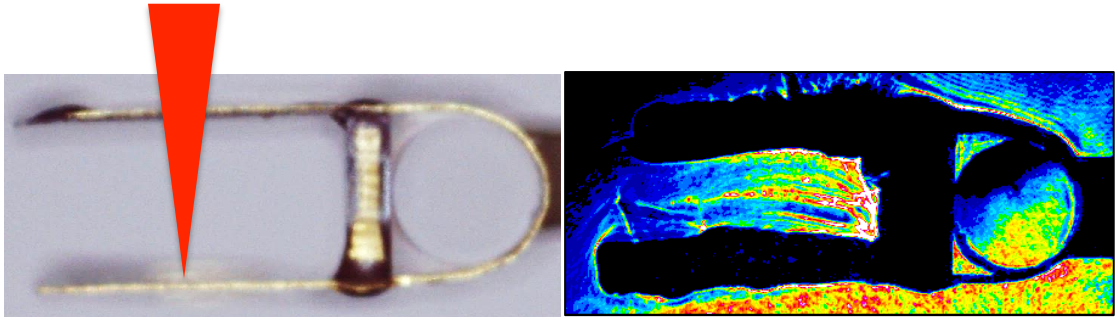

Figure 1: (Left) Geometry for hohlraum (end-view) self-magnetization on Omega-EP, with beampath shown schematically in red. (Right) Sample of 4w probe data used to infer Faraday rotation.

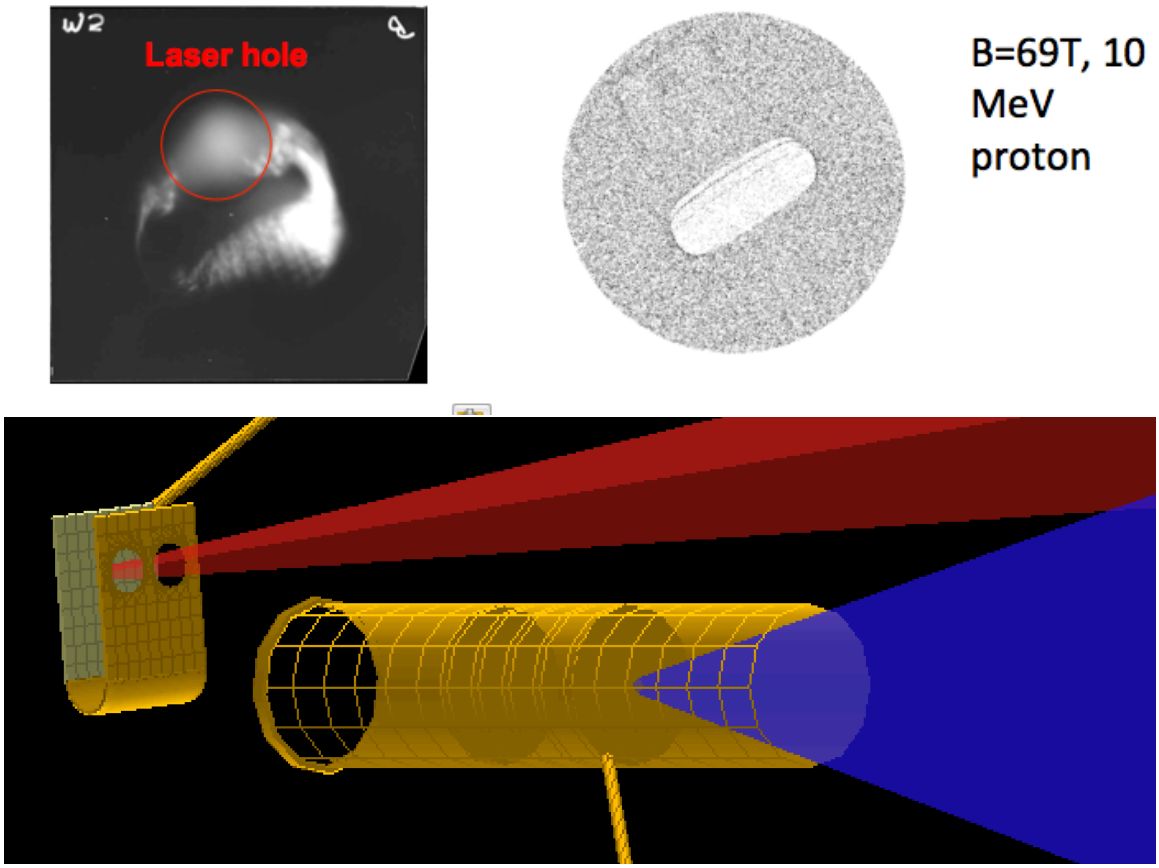

Figure 2: (Bottom) Geometry for proton deflectometry on Omega-EP, with proton detector 15 cm behind the B-field target. (Top right) Sample of proton data with corresponding (top left) analysis of the proton evacuated region; the inferred field along the axis of the loop interior is 69 T.

7. Hohlraum-Free Platform for X-ray Driven Equation of State Measurements (PI: P.M. Celliers)

with D.E. Fratanduono (LLNL), and M. Karasik, S. Obenschain and A. Schmitt (NRL)

The HohlraumFree campaign comprised two shot days on OMEGA-EP during FY15. This campaign performed experimental tests of a hybrid platform for driving planar steady shocks into equation of state target packages. The platform concept combines features of both direct and indirect drive by using a high-Z layer to convert the laser drive into a soft x-ray source in proximity to a low-Z ablator. The ideas behind this concept were proposed by the experimental team based at NRL (Karasik, Obenschain, Schmitt). The high-Z layer is typically of sub-micron thickness, for example a few hundred nm of Au or Pt, followed by a conventional low-Z ablator material (polystyrene or kapton). This drive assembly is then mounted to the EOS package consisting of a reference standard and sample materials. The shot campaigns were aimed at examining the pressure scaling, shock quality and other performance details of this platform, for drive intensities up to 5×10^{14} W/cm^2. For our tests we used a radiation blocking layer of several microns of Cu or Au followed by thick quartz witness samples. The shock transmitted into the quartz was diagnosed with VISAR to determine the drive pressure.

The first experimental campaign encountered significant issues with blanking of the VISAR signals for drive intensities exceeding 2×10^{14} W/cm^2. Analysis of the signals suggested that the blanking was caused by hot electrons circulating around the target package from the ablation plasma. These electrons might deposit enough energy on the rear surface of the quartz witness to render the quartz opaque. The targets were all assembled with 5 mm diameter shield washers, a size that was requested by the facility in order to minimize debris loading in the target chamber. The facility subsequently investigated the blanking issue by testing various shield washer sizes, and found that 10 mm washers should be adequate for most experiments.

The second campaign repeated the scaling experiments using packages fitted with 10 mm washers, and also made adjustments to the laser pulse shape. A complete data set was obtained with enough information to construct a drive scaling curve to help with design of future tests of this platform, both on EP and on the NIF.

8. Broadband Proton Radiography of Shock Fronts in Gases (PI: Y. Ping)

with H. Sio (MIT), G.W. Collins (LLNL), and R. Hua, C. McGuffey, and F. Beg (UCSD)

Two days were dedicated to developing a new experimental platform on Omega-EP to study shock front structure and field effects in low-density systems. The broadband proton backlighter is generated by high-intensity short-pulse interaction with metal foils though the well-known TNSA (target normal sheath acceleration) process. The shock is driven by 3 UV long-pulse beams into a gas cell or freestanding foams. Both shot days provided excellent proton radiographs of shock propagation in gases and foams. Figure 1(a) shows a radiograph from the first shot day, using 5 MeV protons to probe a shock driven by 1.5kJ UV energy in 1ns. A ring structure is clearly observed, indicating accumulation of protons at the shock front, consistent with the existence of an electric field. For the second shot day, the intensity and energy of the proton beam was substantially enhanced by an improved target design and higher short-pulse energy. Using a stronger long-pulse drive (6.2kJ total), a double-shell structure is observed which is proton-energy dependent, as shown in Figure 1(b) and (c). A paper on this new platform is being prepared (H. Sio, et al.) and further analysis of the radiographs is in progress.

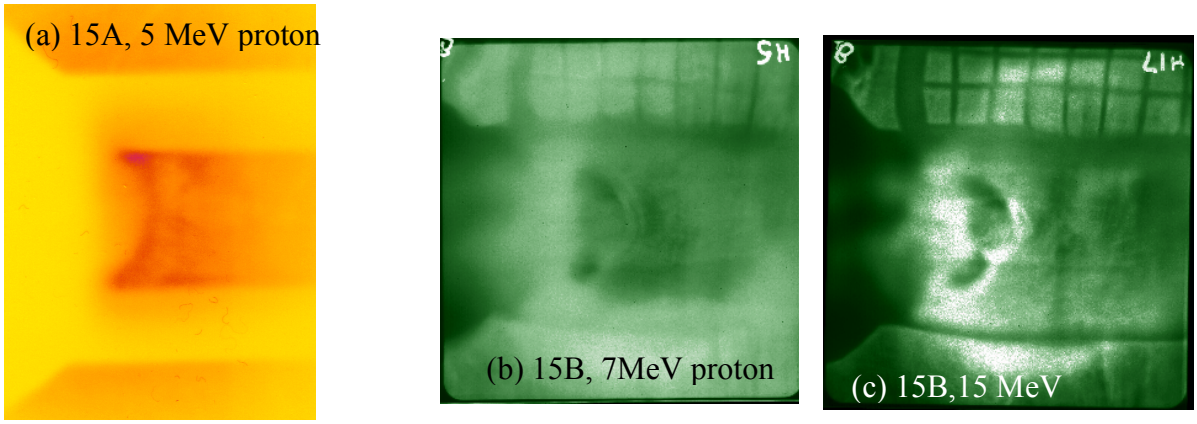

Figure 1: (a) A 5MeV proton radiograph of a gas cell from 15A shots. (b)-(c) 7 MeV and 15 MeV proton radiographs from 15b shots, showing the double-shell structure together with a separate spatial fiducial grid.

High-Energy-Density Experiments

A. Material Equation of State Using Diffraction Techniques

1. Shock Melt and Ramp Re-Crystallization of Tin (PI: R.G. Kraus)
with F. Coppari

The ultra-high pressure melt curve (e.g. >3 Mbar) is a difficult region of phase space to access experimentally. The combined high pressures and temperatures are often out of reach of standard diamond anvil cell techniques. Shock compression to such high pressures generates significantly higher temperatures than are necessary to melt the material. Consequently, this campaign utilizes a recently developed technique to shock the material of interest into the fluid phase and subsequently compress it back into the solid phase, using in-situ x-ray diffraction to confirm the existence of a periodic crystal structure.

One day of Omega EP was used to shock tin to pressures ranging from 65 to 75 GPa (all fully molten initially), and then use a second shock to compress the high pressure liquid tin back into the solid stability field at pressures ranging from 130 to 170 GPa. Pressure induced crystallization from a liquid state was observed on four of the experiments, starting at shock pressures of both 65 and 75 GPa. Figure 1 presents a preliminary summary of the shock-melt-resolidification data in a pressure-entropy phase diagram for tin (based upon Carl Greef's SESAME 2161 EOS). The pressure-entropy space is a useful phase space to interpret these experiments, since nearly all the entropy is generated from the first shock to the principal Hugoniot and the subsequent second shock compression is nearly isentropic. Also include in the figure are data from the previous FY14 campaign on shock melting of tin.

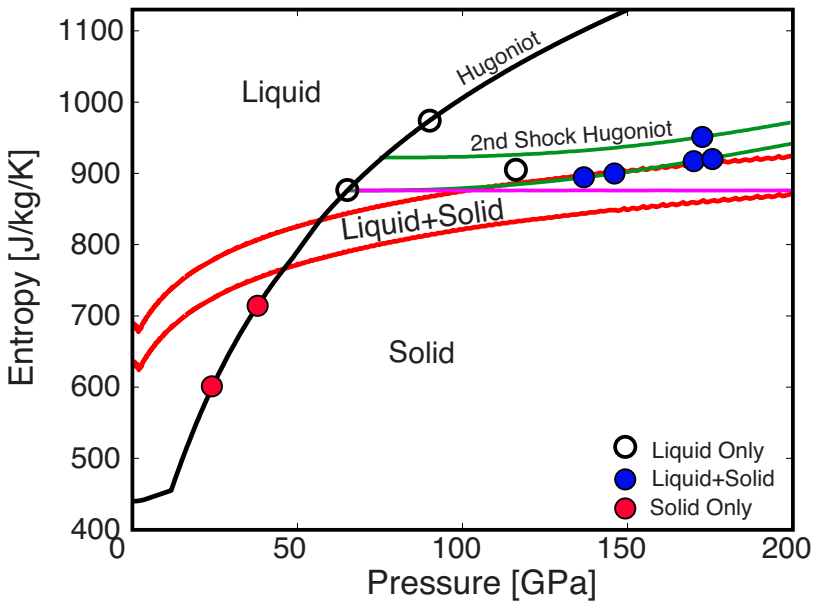

Figure 1: Diffraction data for shock induced melting and re-solidification presented in the pressure-entropy phase diagram for tin. Entropy states are determined from Carl Greef's

SESAME 2161 EOS for tin. Shock compression to the Hugoniot state (black line) increases the entropy and melts tin for shock pressures greater than ~55 GPa. Re-solidification data are plotted along the double shock Hugoniots (green lines), which deviate minimally from the isentropic path (horizontal magenta line).

2. High Pressure Melting of Tantalum As Determined by In-Situ X-Ray Diffraction (PI: R.G. Kraus)

with F. Coppari and D. Fratanduono

The high-pressure melting curve of tantalum has generated significant interest in the high-pressure community, due to the large discrepancy between the static diamond anvil cell experiments and the gas gun shock wave experiments (as diagnosed by sound speed measurements). This Omega half-day campaign investigated the high-pressure phase diagram and also a potential issue with the shock wave experiments: the time dependence of the melting transition in tantalum.

This campaign used the PXRDIP diagnostic to perform in-situ x-ray diffraction measurements of the shocked state of tantalum. In-situ x-ray diffraction is an excellent diagnostic for determining the melting transition, as one can observe the existence of the liquid phase as a diffuse scattering feature, as well as the loss of solid diffraction.

Pressure in the FY15 experiments ranged from 200 to 340 GPa in the tantalum. Figure 1 shows select lineouts from the diffraction data, where one can observe with increasing pressure the loss of solid diffraction lines and the increase in the diffuse scattering feature around the (110) line of BCC tantalum. It is found that incipient melting occurs between ~240 and ~270 GPa and that complete melting occurs between ~300 and ~315 GPa, which is completely consistent with the gas gun data, suggesting that the timescale for shock induced melting is much faster than our nanosecond experiments.

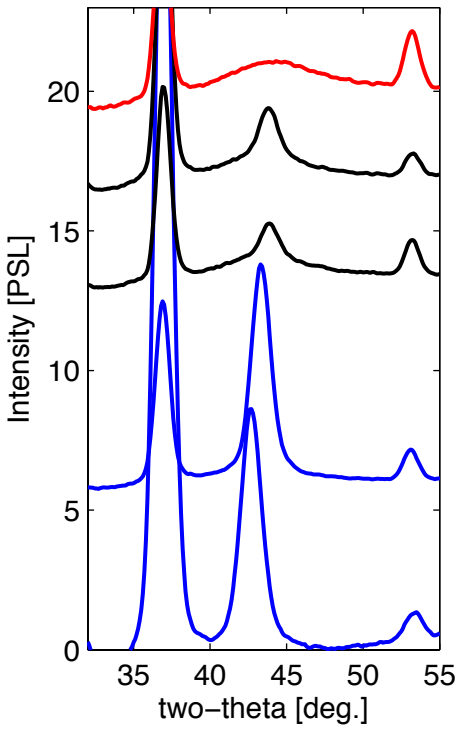

Figure 1: Lineouts from in-situ x-ray diffraction experiments on shocked tantalum. Lines are offset for clarity, where in order from bottom to top the shock pressures were; 202(8), 250(15), 290(14), 307(10), 354(18) GPa. Blue lines represent completely solid, black lines represent solid+liquid, and red lines represent liquid only.

3. Understanding Strength and Structure of Shock-Compressed Diamond
(PI: F. Coppari)
with C. Wehrenberg and J. Eggert

Single crystal diamonds are currently used in powder diffraction experiments performed both at Omega and NIF as ablator and window materials. Understanding diamond's behavior under dynamic ramp-compression, and how strength affects its properties, is crucial to the design of the diffraction experiments and the interpretation of the results.

Models predict that below the Hugoniot Elastic Limit (HEL), diamond is elastically deformed and assumes a strained cubic structure. Above the HEL, plastic deformation should bring diamond back to the cubic structure. What happens to diamond under ramp-compression is currently unknown.

The goal of this first half-day was to demonstrate that Laue diffraction data could be obtained from such a low-Z material, under shock compression. Laue diffraction experiments of diamond, shock compressed below and above the HEL, were performed using the BBXRD diagnostic. Very nice data was obtained (Figure 1) showing differences in the Laue patterns for shocks below and above the HEL. Given the good quality of the data, quantitative data analysis will be possible and will provide a suitable starting point for designing the following ramp-compression experiments.

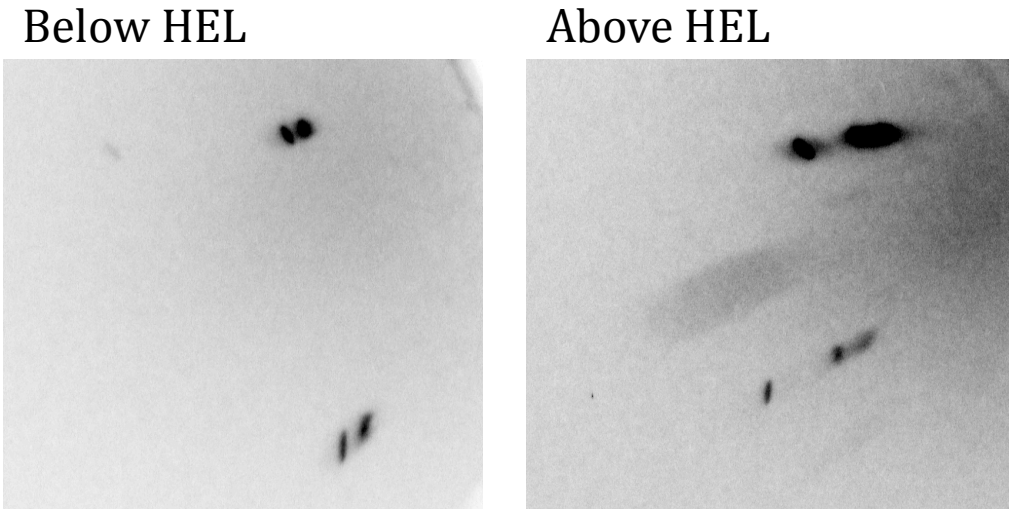

Figure 1: Laue diffraction patterns for diamond shock-compressed below (left) and above (right) the HEL.

4. Development of Germanium X-Ray Backlighters for Diffraction Experiments (PI: F. Coppari)

with J. Eggert and R. Smith

In high pressure dynamic diffraction experiments, the signal/background deteriorates as the pressure increases above ~7Mbar, because of the increase in the background due to the laser ablation. In order to shield this background, metallic filters are used to cover the image plate detectors, whose material (usually) matches the x-ray source. At Omega, Fe (6.7keV) and Cu (8.2keV) x-ray sources were previously developed for diffraction experiments, but these are not optimized for shots in the TPa regime since the ablation X-ray background enters the backlighter energy range and can no longer be filtered. This campaign developed a higher-energy x-ray source (Ge He-alpha at 10.2keV) to improve the signal/background in high pressure shots by enabling more effective shielding of the background X-rays.

This half-day campaign varied the laser intensity used to drive the Ge backlighter, to find the maximum conversion efficiency. Maximum x-ray emission was obtained using a double sided illumination of the Ge foil at an intensity of 9×10^{14} W/cm^2. Figure 1 shows a typical Ge spectrum. These shots also ramp-compressed Fe up to 7 Mbar, to see how the diffraction data are improved in high pressure shots. Figure 2 reports the comparison between two different shots at similar peak pressures, using the old (Cu) and new (Ge) x-ray sources. Measurement quality is improved with Ge backlighter, where the diffraction lines span the entire image plate and are not suppressed by the high background.

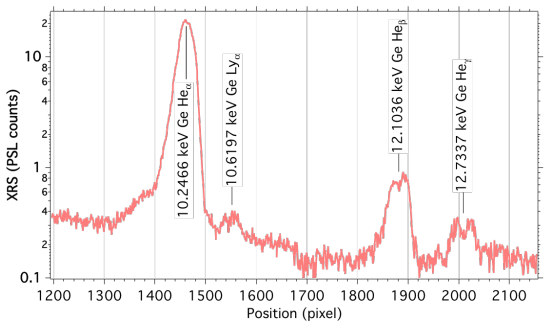

Fig. 1: Typical spectrum emitted by the Ge backlighter, as recorded by the XRS Rowland Spectrometer at Omega.

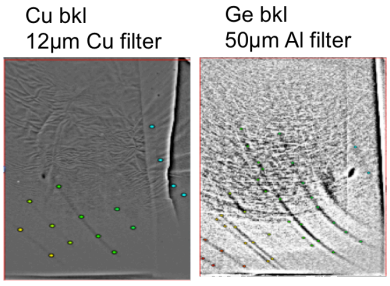

Fig. 2: Comparison of the diffraction signals obtained with Cu (left) and Ge (right) x-ray sources for a similar drive.

5. Shock Melting Transition in Iron as Determined by In-Situ X-ray Diffraction (PI: R.G. Kraus)

with F. Coppari and D. Fratanduono

The high-pressure melting curve of iron is critical to our understanding of the Earth, as it provides a reference point for the temperature deep within the core. This half-day Omega campaign investigated the high-pressure phase diagram of iron, particularly the pressure for incipient melting. It also explored a potential issue with the shock wave experiments, the time dependence of the melting transition in iron. The PXRDIP diagnostic was used to perform in-situ x-ray diffraction measurements of the shocked state of iron. In-situ x-ray diffraction is an excellent diagnostic for determining the melting transition, as one can observe the existence of the liquid phase, as a diffuse scattering feature, as well as the loss of solid diffraction. Pressure in these experiments ranged from 200 to 300 GPa in the iron. This campaign significantly improved the accuracy of the shock state determination, through improved pulse shaping. It was found that incipient melting occurs between ~205 and ~220 GPa, and that complete melting occurs by ~300 GPa. This is consistent with earlier gas gun data, suggesting that the timescale for shock induced melting is much faster than these nanosecond timescale experiments.

6. Understanding Diffraction Signals from Single Crystal Diamond Windows (PI: F. Coppari)

with J. Eggert

Single crystal diamonds are currently used as ablator and window materials in powder diffraction experiments at Omega, Omega EP and NIF. Understanding diamond's behavior under ramp-compression, and its diffraction signal, is critical to correctly interpret diffraction data for other materials, since the measurement includes diffraction from the diamond ablator and window as well as the chosen sample material.

In Bragg diffraction experiments (using a monochromatic x-ray source), one doesn't expect to record signals from single-crystal materials unless the Bragg condition is satisfied for a particular reflection at that wavelength. The resulting diffraction signal is then a localized spot. The Omega and NIF data most often show a very bright, highly textured spot with noticeable broadening in Bragg angle. This feature could be consistent with Bragg diffraction from initially single crystal diamonds, whose symmetry gets partially destroyed by the ramp-compression. But another interpretation could be that this is the diffraction of a highly textured sample material, rather than the diamond window.

To unambiguously assign the observed feature to either diamond or sample, one day of experiments were performed at Omega EP. These reproduced the compression used in past shots, but here the target didn't have any sample material, it was just a bare diamond. Figure 1 shows a representative result. The extended lines are from the Ta pinhole (reference material); the diamond signal is highlighted by the red oval and detailed at right. The signal is characterized by a localized spot corresponding to diffraction from ambient pressure diamond, in addition to a broad and textured peak at higher angle corresponding to compressed diamond. This feature is indicative of the pressure gradient existing in diamond when the x-ray source is turned on.

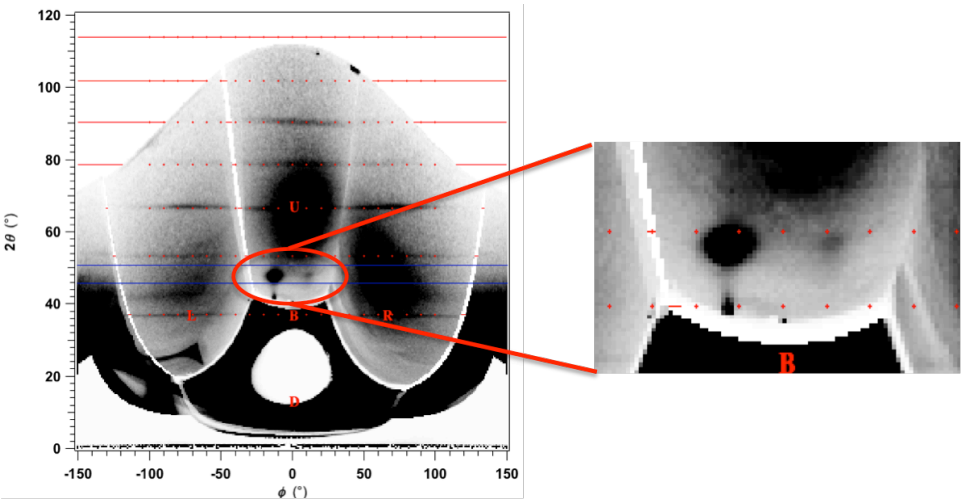

Figure 1: Representative diffraction pattern of ramp-compressed diamond. The straight lines are from ambient pressure Ta used as reference material. The detail at right highlights the characteristic signal due to the diamonds.

7. Development of a Novel X-Ray Diffraction Platform for Constraining the High Pressure Melt Curve (PI: R.G. Kraus)

with F. Coppari

The high-pressure melt curve is tremendously useful for equation of state modeling, as it provides a reference line on the equation of state surface where the free energy of the liquid equals that of the solid. The melt curve is also critical to hydrodynamic modeling, as it defines the boundary between a material with strength and one without. Because of its importance, our team has been developing in-situ x-ray diffraction techniques to determine the high pressure melt curve, including the results presented above from x-ray diffraction of shock induced melting in tantalum and iron, and shock-ramp re-solidification techniques for tin. The campaign described here used one day of Omega EP to develop a novel technique to constrain both the equilibrium high-pressure melt curve and the kinetics of re-solidification. In this platform, a sample is shocked to high pressures, released into the liquid phase, and then re-compressed back into the solid stability field. This campaign also tested a new ablator material for reducing the ablation plasma background. With this novel shock-release-resolidification platform, lead (Pb) was shocked to approximately 50 GPa, released into the liquid phase at ~20-30 GPa, and then re-compressed back into the solid stability field at ~50 GPa. Figure 1 presents data from two image plates showing in-situ x-ray diffraction data from A) shock-released liquid lead and B) shock-released-re-solidified lead. Based upon these preliminary but exciting results, this technique will be useful for constraining the time-dependence of pressure driven solidification and the high-pressure equilibrium phase diagram.

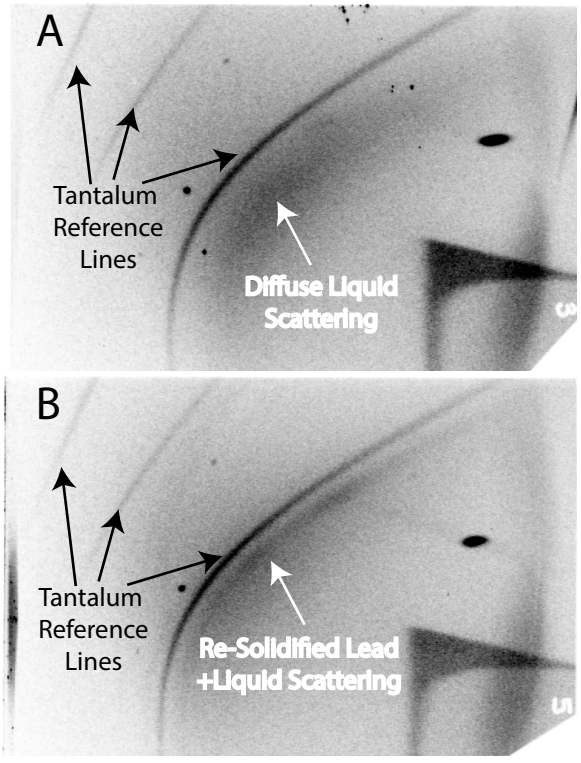

Figure 1: Image plates showing x-ray diffraction from the tantalum pinhole plate (used to reference the image plate location) and from the lead sample. X-ray diffraction in panel A was timed just after the lead sample was shocked to 50 GPa and released to 15 GPa. X-ray diffraction in panel B was timed when the sample was shocked to 50 GPa, released to 15 GPa, and then re-compressed back to 50 GPa. Note: all data and interpretations are preliminary.

B. Material Equation of State Using Other Techniques

1. Measurements of the Lithium Hydride and cubic Boron Nitride Equations of State (PI: A.E. Lazicki)

with F. Coppari, R. London, D. Erskine, D. Fratanduono, D. Swift, P. Celliers, J. Eggert, G. Collins, H. Whitley, J. Castor, J. Nilsen and I. Otero (LLNL)

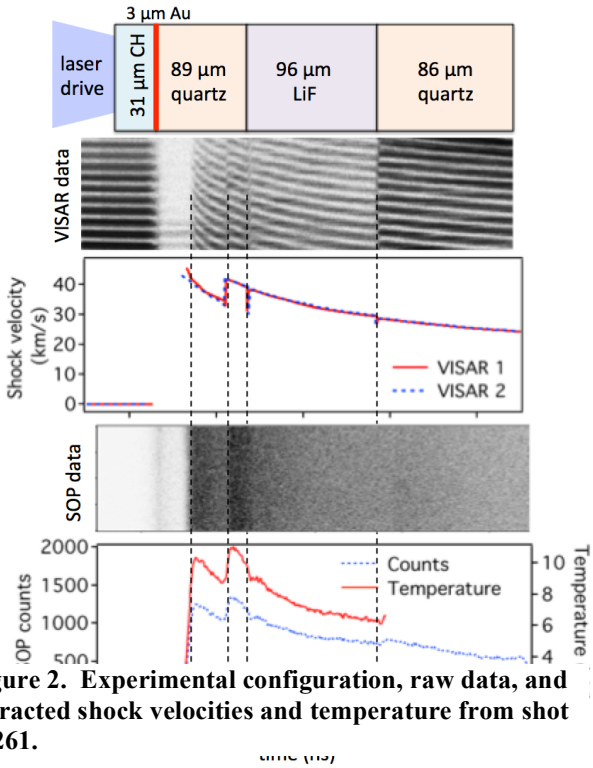

Figure 2. Experimental configuration, raw data, and extracted shock velocities and temperature from shot 75261.

This campaign performed measurements extending the principal Hugoniot of LiF and cubic BN up to the 30 Mbar pressure range, more than doubling the previous high-pressure limit for experiments on these materials. LiF is a common window material in dynamic measurements and potentially useful as an impedance-matching standard and cBN is an ultra-high hardness diamond analog material with important technological applications.

High pressures were exerted using direct (first shot day) and indirect (second shot day) drive of layered planar targets. Measurements were made using the ASBO diagnostic to track *in situ* shock velocities and the SOP diagnostic to collect thermal self-emission. Pressure and density were determined using impedance-matching to quartz (1), and thermal emission from quartz was also used as the standard for determining temperature (2,3). LiF Hugoniot data for one of the shots is shown. Analysis is in progress.

1. M. D. Knudson, PRB 88, 184107 (2013)
2. D. G. Hicks et al., PRL 97, 025502 (2006).
3. M. Millot, et al., Science 23, 347, 418 (2015).

2. Copper and Aluminum Ramp Compression Experiments (PI: D.E. Fratanduono)

In support of ramp compression experiments on the National Ignition Facility (NIF), ramp compression experiments of monolithic aluminum and copper were performed at OMEGA. The goal of these experiments was to test alternate ablators that can be used for ramp compression experiments on the NIF. Over two half days, both copper and aluminum targets were examined. The target design consisted of a vacuum halfraum with a monolithic stepped target (either copper or aluminum) attached to one end of the halfraum. Pulse shapes were designed to produce quasi-isentropic loading of the samples to ~3 Mbar. For the aluminum targets, pulse shaping limitations precluded ramp compression to such pressures, but copper was ramp compressed to 3 Mbar. The experimental results are in good agreement with both ramp compression measurements performed at the Z-machine and the NIF facility. The data were used in the HED materials ramp compression-working group to help guide future NIF ramp compression experiments.

3. Ramp Compression of Single Crystal Diamond (PI: D.E. Fratanduono)

with D. Braun, R. Smith and D. Swift

A half day of single crystal diamond ramp compression experiments were conducted at OMEGA in FY15. Excellent data was obtained on all shots, which have already influenced the design of future TARDIS experiments on NIF. Experiments were conducted as a result of the 2013 High-Z Review. Committee members questioned whether the stress-density response of CVD diamond (polycrystalline) measured by Bradley in 2008 at OMEGA and Smith in 2012 at NIF was adequate for TARDIS experiments that use single crystal diamond. These OMEGA experiments were designed to measure the stress-density response of two diamond crystal orientations (<100> and <110>). A-B comparisons were performed with three different pulse shapes. The goals of the three different pulse shapes were, first, to ramp compress through the Hugoniot Elastic Limit (HEL); second, to shock through the HEL; and third, to test the influence of a gold preheat shield on the ramp profile. Stress-density response was measured in all experiments. Preliminary results suggest that the <110> response is consistent with the CVD results of Bradley. Further, results indicate that the 'pullback' features observed in NIF experiments are significantly reduced in the <110> orientation when compared to <100>. LASNEX has better predictive capability with the <110> orientation vs <100>, but the EOS at high pressure (>100 GPa) needs to be improved. The <110> orientation may obey a simple elastic-perfectly plastic strength model; this is currently being investigated. A-B experiments of <110> vs <100> orientation will greatly assist in our development of a diamond strength model. As a result of these experiments, <110> single crystal diamond will be used in all future TARDIS experiments since the pullback features are greatly reduced.

4. Spherically Convergent Indirect-Drive Equation of State Measurements (PI: A.E. Lazicki)

with D. Swift, J. Hawreliak, F. Coppari, R. London, D. Erskine, D. Fratanduono, P. Celliers, J. Eggert, G. Collins, H. Whitley, J. Castor, J. Nilsen, I. Otero

This FY15 campaign was designed to continue development of the spherically-convergent drive platform on the Omega laser facility, using radiography to track the shock front in a spherical target. The eventual goal of this platform is to measure shock equation of state to the 100 Mbar range, and to establish the Omega facility as a testing ground for platform concepts to be transferred to the National Ignition Facility, where Gbar pressures are attainable. EOS is determined from radiographs, which are recorded (1) on a framing camera, to capture 2-D images from which density and sphericity of the converging shock can be measured; and (2) on a streak camera, to capture the time-resolved shock trajectory from which shock velocity can be determined. In this campaign the converging shock wave was launched using indirect-drive in gas-filled hohlraums into solid balls of CH. Helium-alpha emission from V foils backlit the imploding CH spheres for both cameras. Both diagnostics returned data, and analysis is in progress to inform the design for a second development campaign, which will be focused on optimizing radiographic contrast and collecting data over a longer duration.

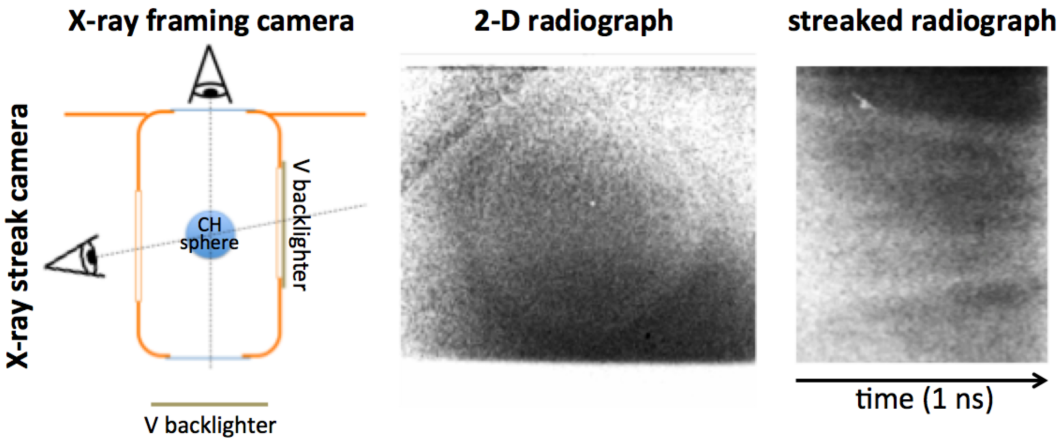

Figure 1. Experimental configuration and raw data from the two primary diagnostics (shot 78284)

5. Development of a Platform for Equation of State Measurements Using Flyer Plate Impact (PI: F. Coppari)

With: D. Fratanduono, A. Lazicki, P. Celliers and J. Eggert

The goal of this campaign is to develop a platform to accelerate diamond flyer plates to hyper-velocity for equation of state measurements. The conceptual design was to ramp compress diamond through direct laser ablation and thereby accelerate the diamond into vacuum. After propagating a known distance, the diamond flyer would impact a transparent diamond window. By measuring the diamond flyer-plate velocity prior to impact and the resulting shock velocity in the diamond witness, the principal Hugoniot of diamond can be determined *absolutely* (e.g. without needing a known pressure reference), enabling the development of diamond as an EOS standard.

This campaign looked to demonstrate this technique and provide EOS measurements in the 10-20 Mbar regimes. In addition, it tested the concept of applying a metal overcoat to the diamond flyer-plate. The purpose of this design is that once the diamond had been calibrated, one could then also determine the metal Hugoniot.

VISAR measurements allowed tracking of the flyer velocity until the impact (occurring at ~11ns in Figure 1) and of the shock velocity into the diamond window until breakout into the vacuum (~12 ns).

This campaign succeeded in accelerating the diamond samples through ramp-compression (with and without the metal overcoat) to velocities in excess of 30 km/s. The shock velocities measured in the diamond window are consistent with previous datasets and correspond to pressures around 15 Mbar.

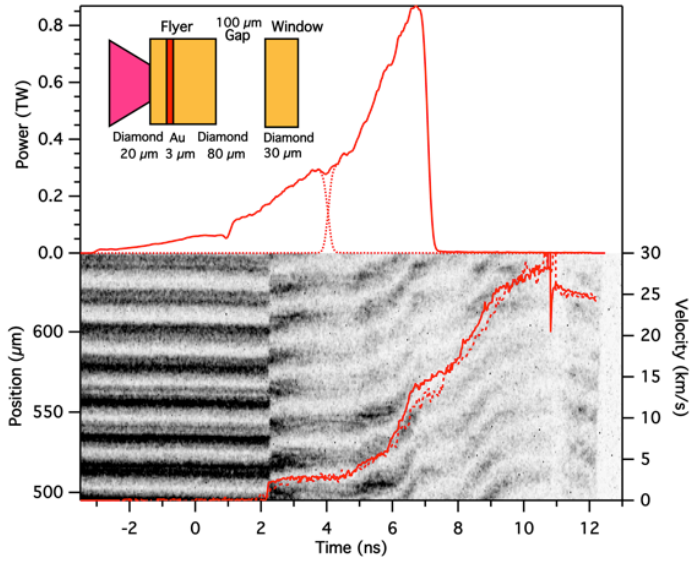

Figure 1: Schematic representation of the target assembly for these shots. The diamond flyer includes a Au layer as pre-heat shield. The experiment used a composite pulse shape (stack of 3 laser pulses) with power increasing over 10ns to gently accelerate the flyer. A typical VISAR trace and velocity profile are shown.

6. Development of a Platform for Extended X-ray Absorption Fine Structure Measurements at the L3 Edge of High-Z Materials (PI: F. Coppari)

With Y. Ping (LLNL)

EXAFS (Extended X-ray Absorption Fine Structure) measurements under dynamic ramp-compression have been proven to be a valuable way of determining the temperature of ramp compressed matter [1]. For high Z materials, the absorption measurements must be performed using the L-edge, because the K-edge would be at too high energy. However, L-edge EXAFS measurements are challenging because the cross section for the absorption event is lower than the K-edge. In order to obtain good quality data given current backlighter capabilities, multiple spectra must be averaged to improve the signal-to-noise ratio. In FY14, prior experiments deployed a multi-channel crystal spectrometer for Ta L3-edge (10keV) EXAFS that enabled simultaneous collection of 5 EXAFS spectra in a single shot [2]. The FY15 campaign extended this technique to measure the EXAFS of Mo at the L3-edge (2.5keV), to take advantage of the higher number of photons emitted by the capsule implosion backlighter at the lower photon energy. A new multi-channel crystal spectrometer (Fig.1) enabled simultaneous collection of 4 spectra per shot, and delivered high quality EXAFS data of undriven Mo in two shots. Figure 2 shows the average over 8 spectra. Data analysis will develop a framework for determining the material temperature from L3-edge EXAFS data.

Figure 1: picture showing the specifically designed multi-channel crystal for the XRS Rowland Spectrometer at Omega.

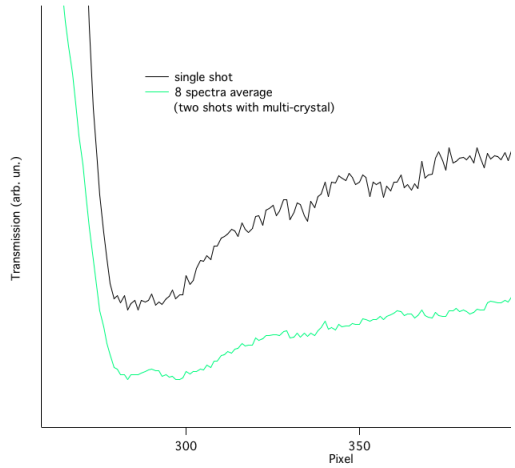

Figure 2: EXAFS spectra of undriven Mo: black single shot, green average over 8 spectra obtained in two shots using the multi-channel crystal.

[1] Ping, Coppari et al, PRL 111, 065501 (2013)
[2] Ping et al, RSI 84, 123105 (2013)

C. Hydrodynamics

1. Mix Width Measurements of Rayleigh-Taylor Bubbles in Opaque Foams (PI: C.M. Huntington)

Foam Bubbles is a new (FY15) OMEGA campaign that aims ultimately to measure the full interpenetration distance ("mix width") of bubbles and spikes in a Rayleigh-Taylor (RT) unstable system. A technique developed over many previous planar RT experiments is the use of a high-opacity tracer-strip, often iodinated plastic, which is located in the center of the physics package and is density-matched to the material around it. When imaged with transmission x-ray radiography, the tracer strip serves to highlight the central features, minimizing the effects of the walls that inevitably exist in shock tube experiments. The tracer strip technique is excellent at providing contrast at the end of the RT spikes, where high-opacity plastic is surrounded by low-opacity foam, but largely obscures the shape and extent of the low-density bubbles, which become mixed with and obscured by the doped tracer material. In contrast, the Foam Bubbles campaign is developing an opaque *foam*, to be paired with a transparent plastic, in order to highlight the extent of bubble penetration across the unstable interface. Ideally, one could use the contrast provided by the doped materials—plastic in one region and foam in another—to measure both bubble and spike length at a single interface, ensuring that the entire system has experienced the same acceleration. This is done using the target shown in Fig 1. (a), which led to the radiograph seen in Fig. 1 (b) for the case without an artificially perturbed interface. The image was generated using tilted, tapered, point-projection x-ray imaging, and clearly shows the layers on each side of the split target. The extent of bubble penetration in an RT unstable system is a fundamental quantity, and this measurement furthers our understanding of hydrodynamic systems from ICF implosions to supernovae.

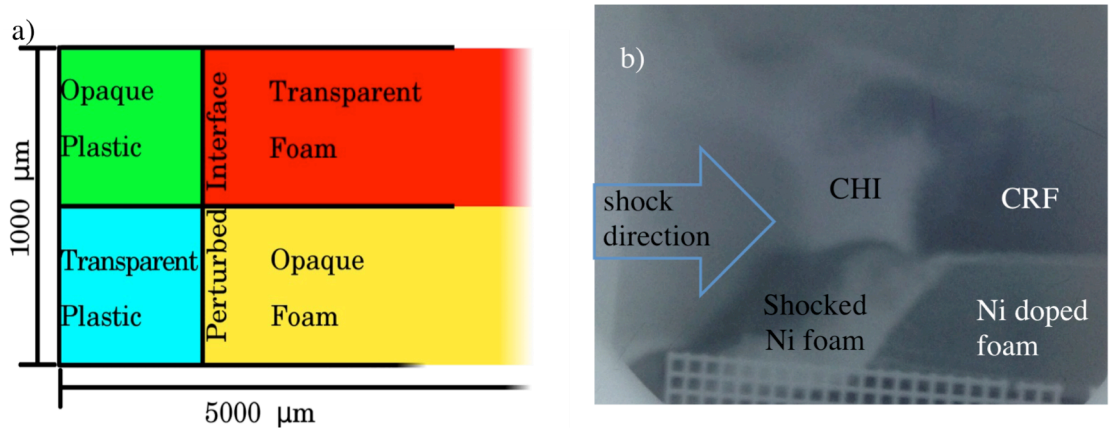

Fig.1 a) Schematic of the target, showing the four regions of heavy / light and opaque / transparent materials. The system is driven from the left. b) An example radiograph, showing the four layers. The shock appears flat in the CHI-CRF, but is distorted in the Ni-doped foam section.

2. Radiographic Techniques for Drive Symmetry (PI: D. Martinez)

Two half-days of hohlraum-driven radiography experiments were performed on the OMEGA laser system in FY15. The primary objective was to investigate the evolution of a driven interface using point projection X-ray radiography. For this campaign the point backlighter was generated through a 20μm pinhole along the "Cranked" TIM 6 axis, and recorded with a single strip XRFC. The experiments were performed over two half day campaigns to qualify the Hohlraum drive, using VISAR for hohlraums on the H7 axis and using Dante for hohlraums on the H10 hohlraum axis. The FY15 experiments were successful, with twelve shots consisting of 4 VISAR shots, 2 Dante shots and 6 radiography shots. Excellent data was recorded on all diagnostics and the experiments met the goals of the HED program.

D. Plasma Properties

1. Thermal Conductivity Measurements of CH/Be by Refraction-Enhanced X-ray Radiography (PI: Y. Ping)

with Amalia Fernandez, Otto Landen and G. W. Collins (LLNL)

This campaign employs differential heating (Y. Ping *et al.*, *Phys. Plasmas* 2015) to generate a temperature gradient, and thermal conduction along that gradient is followed using the technique of time-resolved refraction-enhanced x-ray radiography that has been developed previously on OMEGA. The FY15 shot day obtained 15 shots total. The CH/Be target was heated from both sides by 2 groups of beams, reaching a temperature of ~10 eV, about twice as high as in previous campaigns. High-quality x-ray radiographs have been obtained. Attention was also paid to measure the background and flatfield, which are both critical to normalize the radiographs. It was found that the heating beams produced non-negligible background in the framing camera, even though they were fired outside the gate window and produced x-rays at different energies from the backlighter. This provided an important correction in the refractive fringe contrast. The data will be used to benchmark thermal conductivity models in the warm dense matter regime.

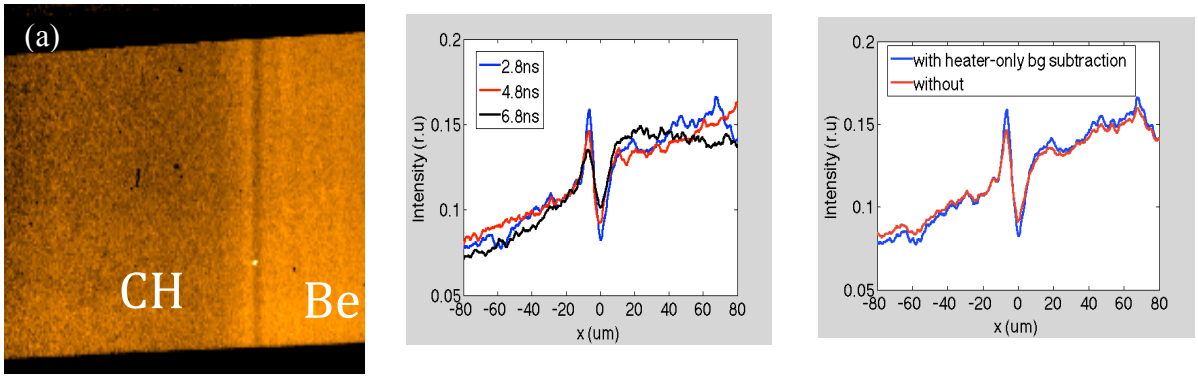

Figure 1: (a) X-ray radiograph of CH/Be interface. The waves propagating away from the interface are also visible. (b) Lineouts of the x-ray radiographs at 3 delays. (c) Correction of the refractive fringe profile due to background induced by the heating beams.

2. X-ray Spectroscopy of Fully Characterized Non-LTE Gold Plasmas (PI: R.F. Heeter)

with G.V. Brown, J.A. Emig, M.E. Foord, D. Liedahl, C.A. Mauche, J. S. Ross, M.B. Schneider, A. Steele and K. Widmann (LLNL) and also D. Froula and J. Katz (LLE).

A more precise understanding of the radiative properties of non-LTE gold is required to improve the fidelity of hohlraum X-ray drive simulations for National Ignition Facility experiments, for both ICF and HED applications. Expanding upon prior work,[1] the FY15 Non-LTE campaign studied X-ray emission from laser-heated beryllium-tamped gold-iron-vanadium foils. The campaign acquired data for four different target types: (a) a "thicker" mixture of Au, Fe and V, (b) a "thinner" mixture of Au, Fe and V, (c) a mixture of Fe and V without Au, and (d) a "null" target with only the 10 micron Be tamper. Data obtained on 12 shots included simultaneous measurements of (1) time-resolved gold M-band spectra from 2 to 5.5 keV, (2) measurements of the plasma electron temperature via K-shell emission from helium-like V and Fe ions, and (3) measurements of the plasma density from time-resolved face-on and edge-on imaging of the sample's expansion from its initial size. For a few targets, an independent measurement of the electron temperature, using Thomson scattering in a transmission geometry, was obtained starting 0.3 ns after the spectroscopic data. Preliminary analysis indicates electron temperatures of 1200 eV were obtained in the FY15 shots, as on the FY14 series (Figure 1). Ongoing detailed analysis is expected to lead to improved validation benchmarks for non-LTE models.

1. R.F. Heeter *et al.*, *Phys. Rev. Lett.* **99**, 195001 (2007).

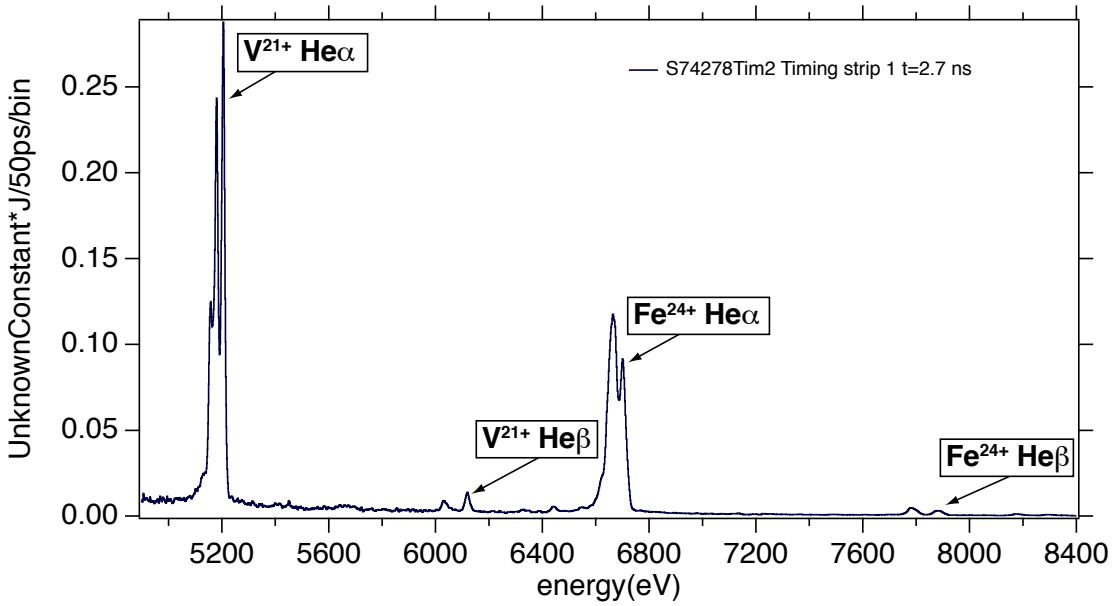

Fig1: Spectrum measured by the MSPEC spectrometer of the X-ray emission from K-shell transitions in highly charged vanadium and iron. An electron temperature of 1200 eV is inferred from the various line ratios. Multiple shots in 2014 and 2015 delivered nearly identical data.

3. Magnetized Collisionless Shocks for Weapons Effects (PI: B.B. Pollock)

with H.-S. Park, J.S. Ross, C. Huntington, and G. Swadling

In FY15 this new campaign on Omega began an investigation of interpenetrating plasma flows in the presence of background magnetic fields. The first shot day employed the MIFEDS pulsed-power magnetic field system to provide a background field along the direction of a low density plasma plume produced inside the MIFEDS structure, into which a separate, orthogonal, high density plume was driven after a variable delay. Figure 1 illustrates the experimental setup. The plasma interaction region was probed with both second-harmonic optical Thomson scattering and D-^{3}He proton deflectometry to measure the plasma density, temperature, flow velocity, and the field structure. The second shot day increased the density and temperature of the plasma along the MIFEDS axis by incorporating additional drive laser beams, and also looked at head-on collisions from opposing flows along the MIFEDS axis (in addition or separately from the orthogonal plume). The analysis of this recent experiment is ongoing and will inform the FY16 continuation of this effort.

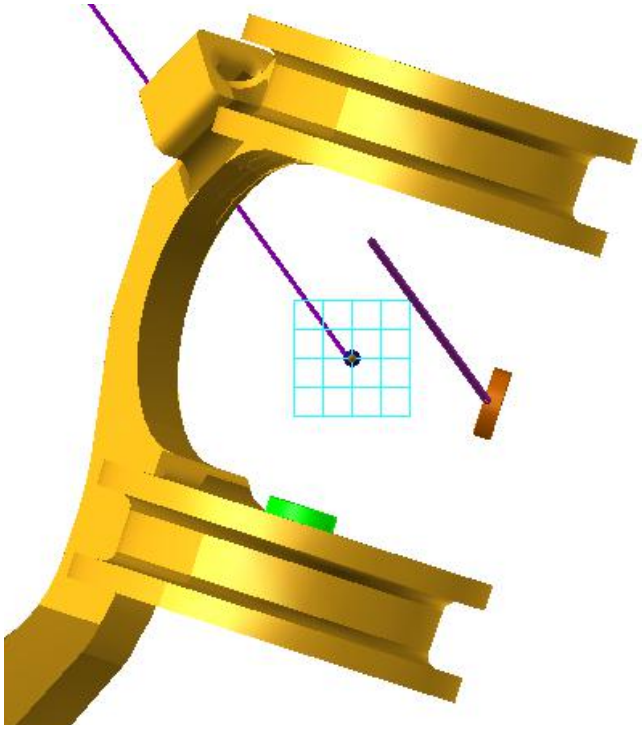

Figure 1: The MIFEDS used in this campaign. The green disk on the lower surface is illuminated by 2-8 beams, producing one of the plasmas along the MIFEDS axis. The gold-colored disk on the right provides the orthogonal plasma plume. The Thomson scattering volume is at the intersection of the surface normal for these disks. The blue gridded region shows the field of view for proton backlighting, using protons produced by imploding the D-^{3}He capsule positioned behind the grid.

4. Fusion Product Stopping Power Measurements in Plasmas (PI: J. Frenje, LLNL/MIT Collaboration)

The motivations for the one-day FY15 Plasma Stopping Power campaign on Omega were, first, to measure plasma stopping power around the Bragg peak to validate different theories for varying plasma conditions (for the first time), and second, to measure ion-electron (i-e) equilibration rates to experimentally validate the Coulomb logarithm for various plasma conditions (also for the first time in this regime). Observations and conclusions from these 12 shots are as follows: Charged-particle data obtained with the CPS1, CPS2 and WRF spectrometers clearly indicate that the plasma-stopping power around the Bragg peak varies with plasma conditions (Figure 1). The data is well modeled by the Brown-Preston-Singleton stopping-power formalism. X-ray streak camera and gated x-ray imaging data were also obtained, from which $n_e(t)$, $T_e(t)$ and $n_e(r,t)$ and $T_e(r,t)$ data will be inferred that is essential for constraining plasma-stopping-power modeling. A second framing camera imaged the shell location versus time; the 3MLARD neutron detector provided clean measurements of the secondary-neutron yield (hard x-ray levels insignificant as designed), which provide fuel ρR data also used for constraining the plasma stopping power modeling. The data quality should be good enough to validate the stopping power around the Bragg peak. The observations and conclusions resulted in an invitation to present these results at the 2015 APS-DPP meeting. Fig. 1 shows the stopping power for three different plasma conditions.

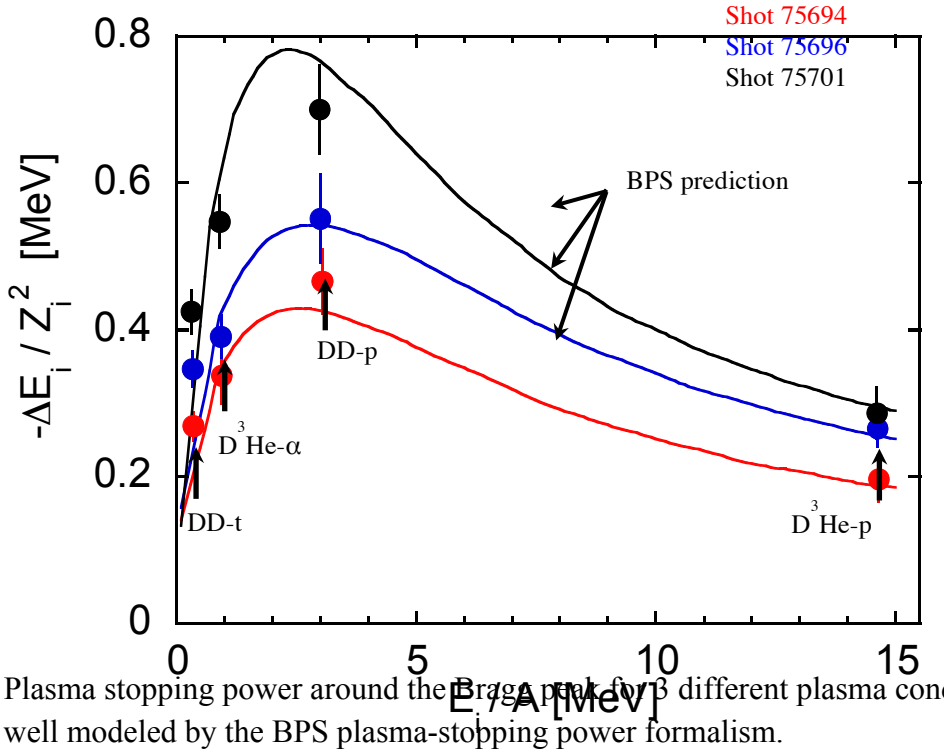

Fig. 1. Plasma stopping power around the Bragg peak for 3 different plasma conditions (3 shots). The data is well modeled by the BPS plasma-stopping power formalism.

E. Material Dynamics and Strength

1. Copper Rayleigh-Taylor Growth (PI: J.M. McNaney)

with S. Prisbrey, H.-S. Park, C.M. Huntington and C.E. Wehrenberg

The Copper Rayleigh-Taylor (CuRT) campaign is part of the Material Strength effort aimed at assessing the strength of various metals at high pressure and high strain rate. The goal of the CuRT platform is to measure Rayleigh-Taylor (RT) growth of samples that behave "classically," which is to say they can be fully modeled using a fluid description. In this series of experiments the intent is to measure RT growth in liquid copper at high pressure. An additional goal is to demonstrate the dynamic range of the technique by measuring RT growth in solid copper.

Without the stabilization of strength, classical RT growth is characterized by a growth rate $\gamma = \sqrt{kgA_n}$, where k is the wavelength of the unstable mode, g is the acceleration, and the Atwood A_n number quantifies the density jump at the interface. Acceleration of the sample in the experiment is provided by the stagnation of a releasing shocked plastic "reservoir," which is directly driven by 1 to 2 kJ of laser energy, depending on the desired material condition. The growth of pre-imposed ripples is recorded using transmission x-ray radiography from a copper He-α slit source, where the opacity of the sample is calibrated to the ripple amplitude. The pre-shot metrology and measured ρr of the driven sample together yield the growth factor, which is compared to models of RT growth. Diagnostic features allow same-shot, in situ measurements of the modulation transfer function (gold knife edge on sample) and the opacity look-up table (copper step filters on the imager), resulting in error bars of roughly ±10%.

Three shot days on Omega-EP were fielded in FY15, first to develop the drive conditions necessary to produce both liquid and solid copper, and then to produce two sets of RT measurements. In the first set of RT measurements, post-shot simulations indicated that the copper sample was in a mixed solid-liquid state. Initial data for solid copper was obtained on the second in second set of RT measurements. Analysis of these Q4 shots has just begun, but an example of the experimental data is shown in Figure 1. There is contrast from both the driven (center) and undriven (edges) regions.

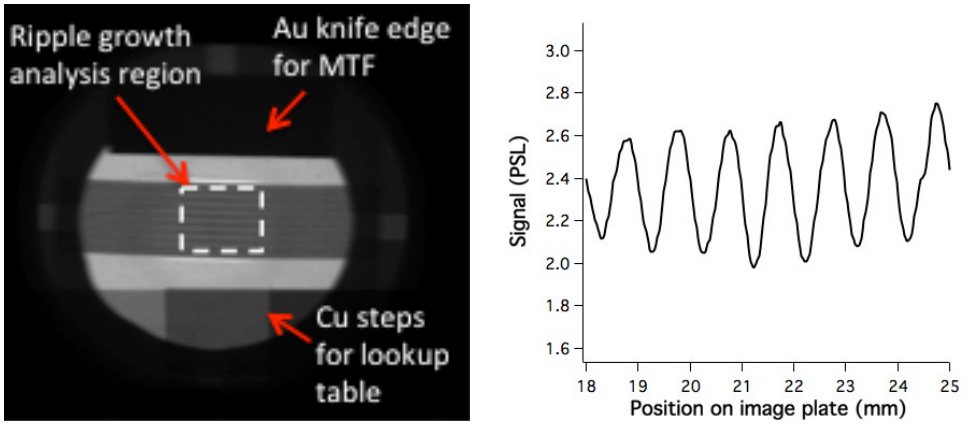

Fig. 1. The radiograph from Omega-EP shot 21025 is shown at left, and a lineout taken from the middle of the white box is plotted at right.

2. Measurements of In-Situ Strain in Shock Compressed Single-Crystal Tantalum (PI: C.E. Wehrenberg)

The primary goal of this Omega-EP campaign was to record a time series of diffraction patterns for single-crystal Ta shock compressed along the [001] direction at 0.5 Mbar. 1 UV beam drove a CH/Ta/MgO crystal package with a 3 ns pulse and a 2mm phase plate, while a 100 ps IR pulse was used to drive the Zn backlighter. Driven diffraction signals were successfully recorded for three different backlighter delays, spaced 0.4 ns apart. In addition two drive shots were performed to confirm the repeatability of the 0.5 Mbar drive. One secondary goal for this shot day was to develop transmission Bragg diffraction on Omega EP. To this end, two shots were performed, a background shot and a transmission shot, using EP's other 2 beams, and these will inform the design of future transmission Bragg experiments. Figure 1 presents lineouts from the diffraction data, showing a consistent strain measurement for different timings of 0.5 Mbar shock loading experiments.

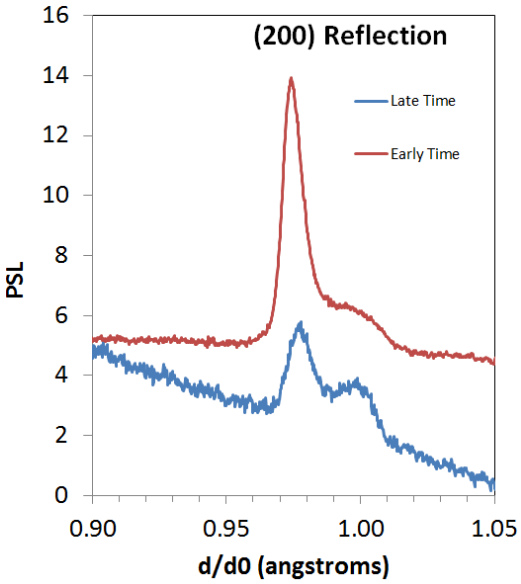

Figure: Lineouts from reflection diffraction data plotted as a ratio of driven d-spacing over ambient d-spacing, d/d_0, for two 0.5 Mbar experiments.

3. Understanding the Basic Plasticity Mechanism in Shock Compressed Tantalum (PI: C.E. Wehrenberg)

One Omega-EP shot day was dedicated to the first campaign seeking to detect plasticity via twinning in shock compressed Ta. Since twinning produces a reorientation of the lattice in a known manner, twinning would produce a change in texture spots on the diffraction ring. This study used vapor deposited Ta samples with a sharp (110) fiber texture, so that any change in texture would produce a marked contrast in diffraction patterns. To observe this change in texture, the TwinDiff campaign used high-energy powder diffraction (16 keV Zr backlighter) to successfully record the entire Debye ring. A new target mounting system was developed and successfully tested which allows samples to be mounted at a 30 degree angle, while performing simultaneous VISAR measurements using a folding mirror. A total of ten shots were performed with shock pressures in the 0.5-2.0 Mbar range. While the lower conversion efficiency of the high-energy backlighter limited the signal-to-noise ratio of the driven signal, it is now possible to track the pattern of the texture spots on the Debye ring to specific texture orientations, (110) fiber texture in this case.

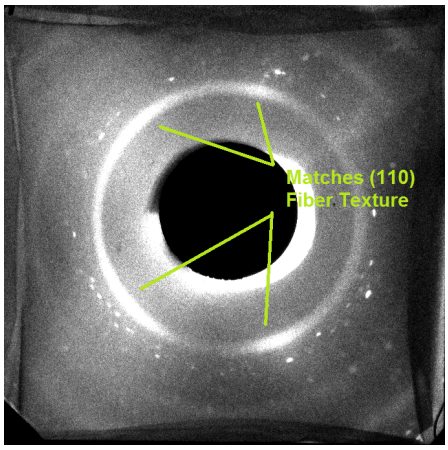

Figure: Diffraction pattern from (110) fiber-textured Ta during 0.5 Mbar shock compression.

F. X-Ray Source Development and Application

1. Optimizing X-ray Emission from Nanostructured Copper Foams (PI: K.B. Fournier)

The FY15 Nanostructure shot day was the culmination of a series of experiments with ultra-low-density foams that had increasing concentrations of metal dopants. The FY15 shots fielded, for the first time, a pure-metal foam that had a density low enough to allow supersonic laser propagation, which resulted in heating nearly the entire target volume to high temperatures. The purpose of the on-going Nanostructure campaigns is to maximize the yield and to tune the x-ray output from high-temperature plasmas using different metallic emitter ions. Maximization of the x-ray yield is achieved by suspending the emitting ions in an ultra-low-density foam matrix, made either of silica aerogel or carbon nanotubes. When the electron density in the aggregate foam material is in the range of 10 – 20% of the critical electron density for the laser light ($n_{cr} \sim 10^{22}$ cm^{-3} in the case of 351 nm laser light), then the entire volume of the target is heated supersonically to multi-keV temperatures. The resulting volume of high-temperature plasma emits K-shell x-rays from mid-Z dopant ions (Ti, V, Fe, Ni, Cu, Ge). The foam targets developed in the past have had target densities in the range 3 – 10 mg/cm^3, and metallic ion concentrations in the range 3 – 20%. [1-5] But for the FY15 shots, targets became available that were 100% Cu (Z=29) with densities in the range 14 – 25 mg/cm^3. While these densities were somewhat too high to have strongly supersonic laser propagation, they were still low enough to achieve nearly full-volume heating of the target. The resulting laser-to-x-ray conversion efficiency in the range of the K-shell x-rays from Cu^{27+} and Cu^{28+} (8 – 10 keV) is approximately 2%, which is a significant enhancement compared to 0.8% for emission in same x-ray energy range from a solid copper disc under the same laser drive conditions. Next steps in this campaign are to achieve even lower foam densities, for better laser coupling and more efficient x-ray production, and to fabricate foams for NIF scale experiments.

[1] K.B. Fournier *et al.*, *Physical Review Letters* **92**, 165005 (2004).
[2] K.B. Fournier *et al.*, *Physics of Plasmas* **16**, 052703 (2009).
[3] F. Pérez *et al.*, *Physics of Plasmas* **19**, 083101 (2012).
[4] F. Pérez *et al.*, *Physics of Plasmas* **21**, 023102 (2014)**.**
[5] F. Pérez *et al.*, *Physics of Plasmas* in press 2015.

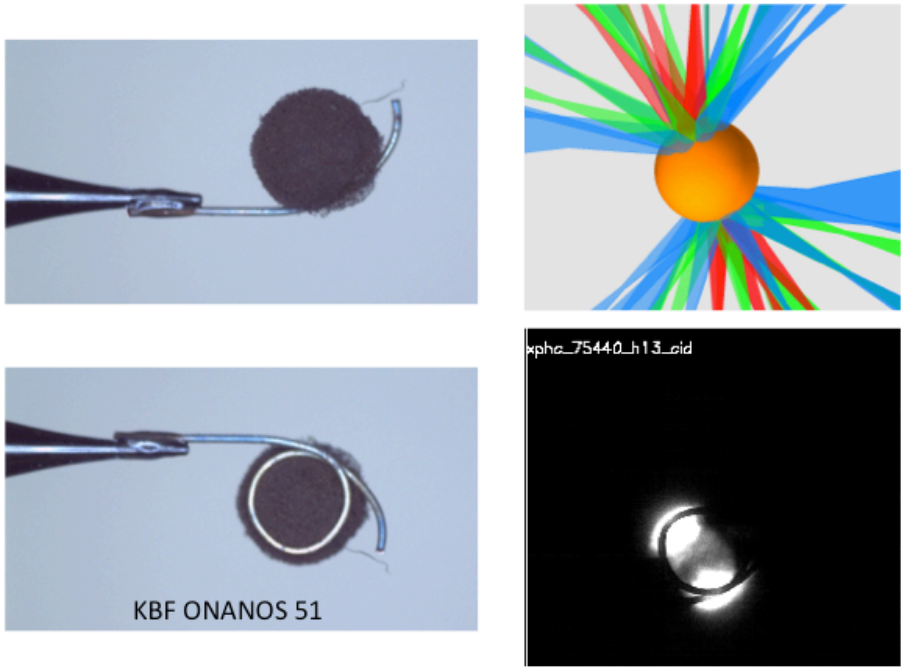

Figure 1 - (left) Photographs of a 14 mg/cm^3 copper foam target mounted for OMEGA shots. (right upper) Nominal OMEGA laser beam pointing at the opposing hemispheres of the foam targets and (right, lower) an x-ray pinhole camera in the light of Cu K-shell x-ray emission showing the two heated faces of the target, and the shadow of the mounting wire used to produce the target.

2. X-ray Source Fluence as a Function of Viewing Angle (PI: M.A. Barrios)

The National Security View (NSView) Omega campaigns study target fluence as a function of viewing angle for x-ray source applications. Our goal is to improve the current understanding of the fluence delivered to material samples and other test objects using these or similar targets as X-ray sources. A previous campaign in FY14 measured the x-ray emission of stainless steel (SS) lined cavities using three different beam axes (H5-H16, P2-P11 and H7-H14) resulting in view angles of 0°, 42°, and 79°, and 5°, 46°, and 75°, for Dante and DMX spectrometers respectively. The two FY15 campaigns continued this work, using the same beam axes to study the x-ray fluence of Fe-aerogel targets having different heat propagation properties than SS lined cavities. In the second campaign, both SS and Fe-aerogel targets were also studied at intermediate angles (37° and 71° for Dante, and 37° and 66° for DMX), by using P5-P8 and H6-H15 beam axes.

Figure shows representative time integrated spectra for (a) SS lined cavities and (b) Fe-aerogel targets. Data from the FY15 campaigns are consistent with findings from FY14, showing little variation in the observed x-ray emission from Fe K-shell, consistent with a volumetric emitter that is optically thin and independent of viewing angle. A larger variation in the Fe K-shell is observed for the aerogel targets compared to the SS targets, likely due to small variations in foam density and microstructure. Larger variations in the x-ray fluence as a function of view angle are observed for sub 2-keV X-rays. Figure and Figure show target total x-ray yield as a function of view angle, compiling data from all campaigns to date, for SS lined cavities and Fe-aerogel targets respectively. As shown in Figure , the total x-ray yield is dominated by sub-2keV emission corresponding to the Fe L-shell, thus the measured total yield is a good indicative of the sub-2keV target behavior. The SS cavity data (Figure) shows a sharp decrease in measured yield below ~30°, not observed in the aerogel targets (Figure). The behavior of the Fe aerogel targets is consistent with a volumetric emitter, once geometric and optical-depth corrections are considered. Such is not the case for the SS lined cavities, which are best described by a surface emitter, with the emission originating from the cavity inner walls and LEH. A spectral reconstruction model was developed to match observations for the SS lined cavities, shown in Figure as the dashed purple and dotted blue lines. For comparison we show a model fit where only geometric corrections are accounted for, shown as the black solid curve. Future work will focus on further development of models to best describe the measured behavior for both types of targets.

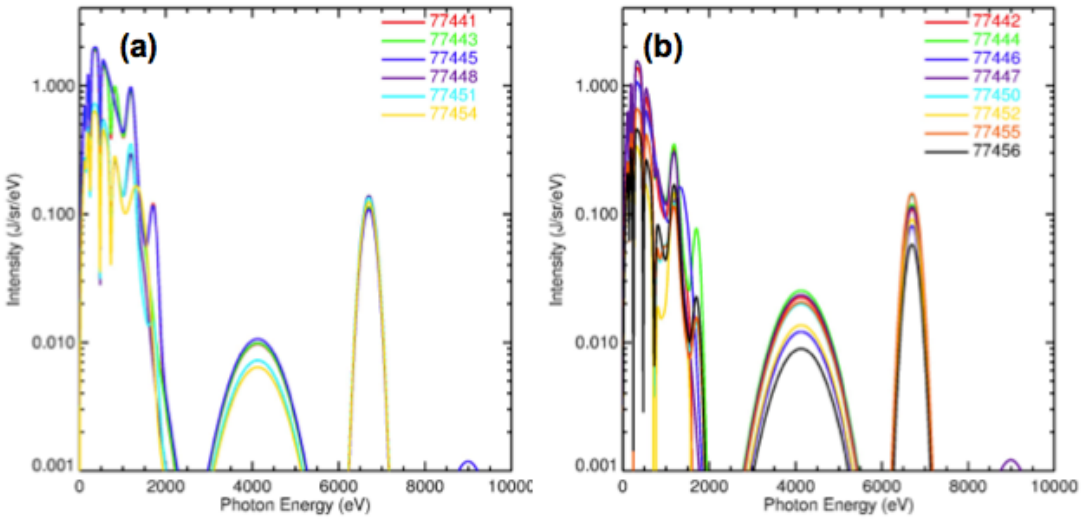

Figure 1: Measured Dante time integrated spectra for (a) Stainless Steel lined targets and (b) Fe- aerogel targets from the second FY15 campaign.

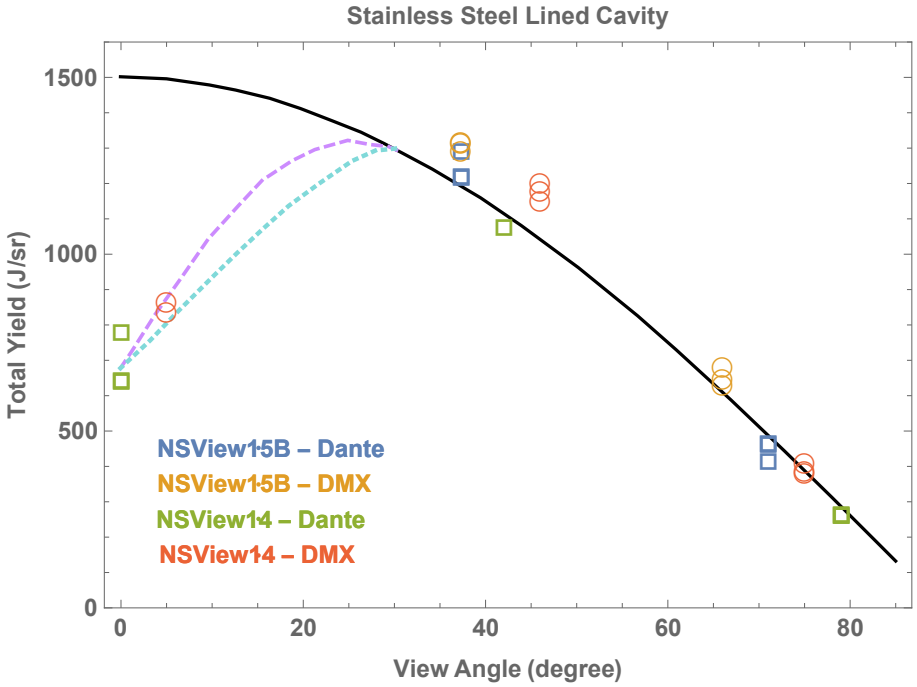

Figure 2: Total X-ray yield for stainless steel lined cavity targets as measured using Dante and DMX spectrometers.

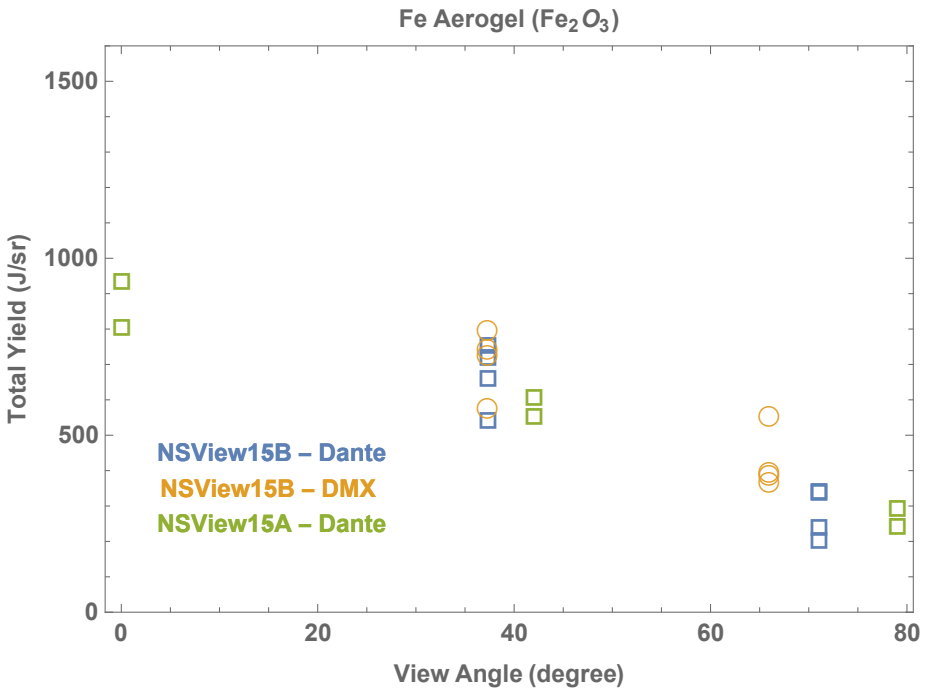

Figure 3: Total X-ray yield for Fe aerogel targets as measured using Dante and DMX spectrometers.

3. Solar Cell Electrostatic Discharge Experiments (PI: K. Widmann)

The overall goal of the SolarCellESD campaign is the development of a large area solar-cell array cold x-ray exposure test platform that can be used to test the response of in-flight solar cells to a simulated nuclear weapons threat environment. In the two SolarCellESD campaigns in FY15, a new x-ray source was developed and tested. The x-ray source was a high-temperature gold halfraum, 600µm in length and 600µm in diameter, which included a small pinhole in the closed end of the halfraum in order to limit the total flux emitted by the source without altering the spectral content. Figure 1 shows a sketch of the halfraum target with the view angles for Dante, which was used to characterize the obtained x-ray radiant power and spectral intensity emitted by the halfraum target, and for one of the two X-ray Langmuir Probe Detectors (XLPDs) specifically designed for the SolarCellESD effort. The XLPDs contain four Langmuir probes and an array of two solar cells. The first XLPD had a view of the pinhole and, thus, was exposed to the cold x rays, while the second XLPD had a view of the hohlraum wall and was mainly illuminated by hard x rays. Initial results from both the Langmuir probes and the solar cells on both XLPDs revealed that sustained arcing was observed and, moreover, that for the low-flux conditions, the discharge was quenched within a few microseconds of the onset of the discharge.

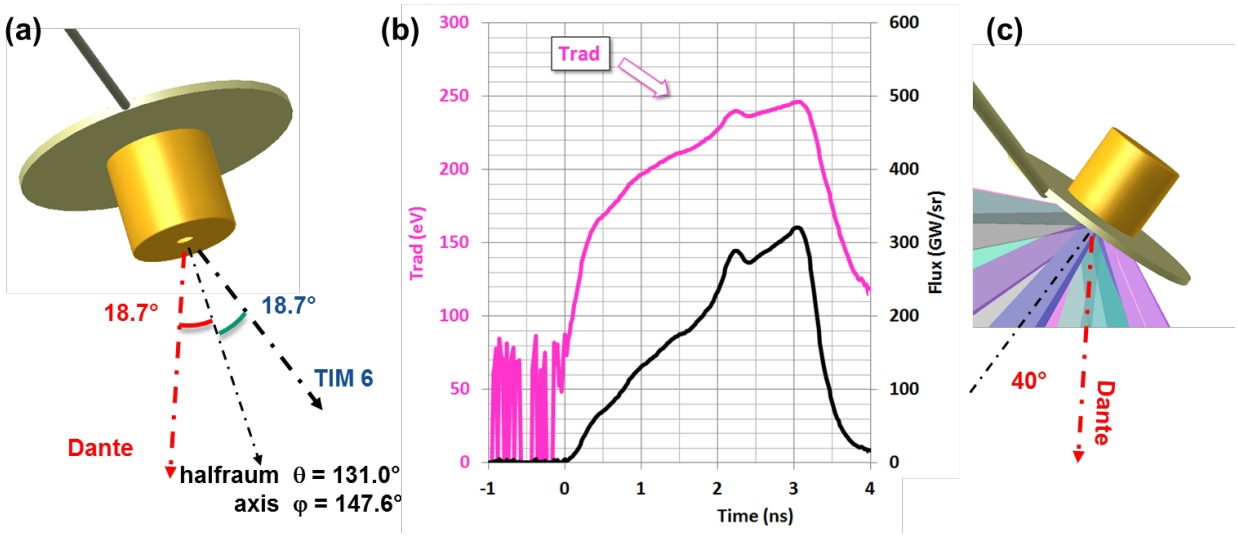

Figure 1: (a) Sketch of the gold halfraum target and view angles for Dante and TIM 6 which was used for one of the X-ray Langmuir Probe Detectors. (b) Dante measurements from a halfraum target that was positioned such that Dante had a view of the "open" side of the halfraum – see panel (c). The 1-ns beams were stacked in time to provide x-ray emission with approximately 3 ns duration.

Laboratory Basic Science Experiments

1. Crystal Structure of Shock Compressed Magnesium Oxide (PI: R. Smith)

Two half-days on Omega-60 and one full day on Omega-EP were dedicated to experiments to shock compress MgO samples to sample pressures from 200-800 GPa, and measure the crystal structure of the shock-compressed MgO using recently developed nanosecond x-ray diffraction techniques [1]. The pressure-temperature phase map for MgO is shown in Fig. 1 along with the predicted shock compression path (Hugoniot). A predicted B1-B2 phase transformation is expected to occur between ~350-450 GPa. The target design shown in Fig. 2 consists of a 100 µm CH ablator, 50 µm MgO and 50 µm Quartz. Using the Omega pulse shape sg3702 or the Omega-EP pulse shape ERM99V012 a steady shock was ablatively driven into the sample. Once the shock has compressed the MgO sample a second sets of laser beams was used to generate a ns source of He-alpha quasi-monochromatic line radiation (8.3 keV). The x-rays scatter off the compressed MgO and the resultant diffraction pattern is recorded on the PXRDIP image plates. A stereographic projection of typical x-ray diffraction pattern is shown in Fig. 3. This information is then used to constrain the MgO crystal structure at pressure. Pressure in the MgO sample during the x-ray probe time is determined by the VISAR diagnostic. The VISAR records the reflecting shock velocity in the Quartz window. Hydrocode simulations matched to this shock velocity are then used to determine the pressure in the MgO sample at the x-ray probe time.

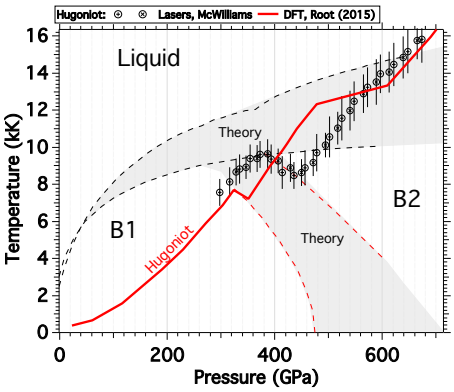

Figure 3. Pressure-Temperature phase map of MgO.

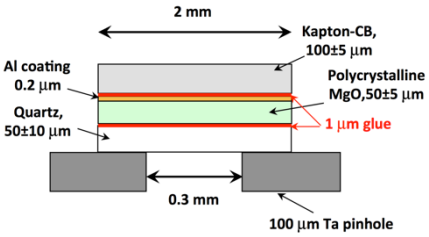

Figure 2. Target design for MgODiff-15A, -15D and MagODiff-EP-15A campaigns.

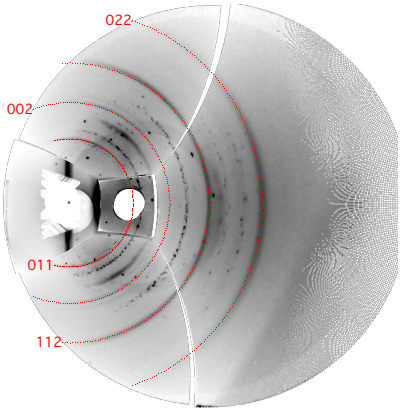

Figure 3. Stereographic projection of the Omega PXRDIP diagnostic [1] x-ray diffraction image plate data.

[1] J. R. Rygg, J. H. Eggert, A. E. Lazicki, F. Coppari, J. A. Hawreliak, D. G. Hicks, R. F. Smith, C. M. Sorce, T. M. Uphaus, B. Yaakobi and G. W. Collins, "Powder diffraction from solids in the terapascal regime", Rev. Sci. Instrum. **83**, 113904 (2012).

2. Structure of Solid and Superionic Water at Uranus' and Neptune's Core Conditions (LBS PI: J.R. Rygg; Shot PI: F. Coppari and M. Millot)

This half-day on Omega-60 completed the FY14 investigation of the structure and equation of state of solid and superionic warm-dense water at Uranus' and Neptune's core conditions, with new laser dynamic compression techniques, optical diagnostics and x-ray diffraction on Omega. Water has a complex phase diagram, characterized by different solid structures, including superionic phases. Superionic water ice is characterized by fluid-like diffusing protons within a solid lattice of oxygen ions. Its existence in the deep interiors of icy giant planets would have a dramatic impact on their internal structure and evolution.

Multishock compression of water allowed us to compress initially liquid water into solid and superionic ices up to 5 megabars while keeping the temperature below 0.5 eV. Streaked optical reflectivity, pyrometry and interferometric Doppler velocimetry (VISAR) as well as x-ray diffraction provided an unprecedented insight on the equation of state, structure of solid and superionic megabar water ices. This is the first time that diffraction data of such a low-Z material have been collected to these extreme conditions.

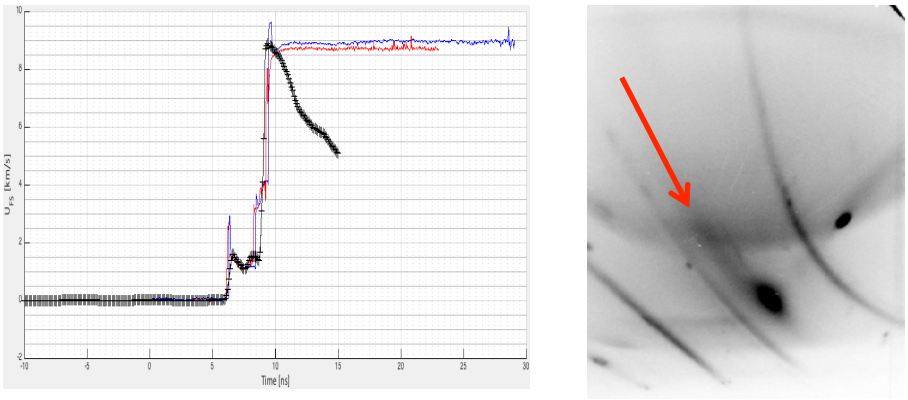

Figure: Left: VISAR traces (red and blue) together with hydrodynamic simulations (black) matching the experimental records. Right: diffraction data showing lines from the Ta reference, the diamond window and solid water (red arrow).

3. Extended X-ray Absorption Fine Structure Measurements of Iron Melting Temperature at Earth's core conditions (LBS PI: Y. Ping; Shot PI: M. Beckwith)

with R. Kraus, F. Coppari, J. Eggert, G. Collins, and T. Duffy

The melting temperature of iron at high pressure is a key for developing reliable thermal models of the deep Earth. This two-day Omega-60 campaign used the previously developed EXAFS platform to obtain high-quality EXAFS data of compressed Fe up to 200 GPa along the Hugoniot. Both days used a dual drive with 37 beams on the backlighter, which worked well and will allow for more flexibility in pulse shaping for future campaigns. The 14 shots in the first campaign were complicated by target issues and unexpected differences in nominally identical spectrometers. The 13 shots on the second day were successful, with good EXAFS and VISAR data obtained on all shots that day. Figure 1 shows a sample image from the multi-crystal XRS array used to collect the Fe EXAFS data, and Figure 2 shows a sample of raw VISAR data. The EXAFS data, together with VISAR data obtained under the same conditions, will provide high-accuracy temperature measurements with error bars substantially smaller than previous data.

Figure 1. Raw image from the multi-crystal XRS array. The Fe K-edge is clearly seen in 4 of the 5 channels.

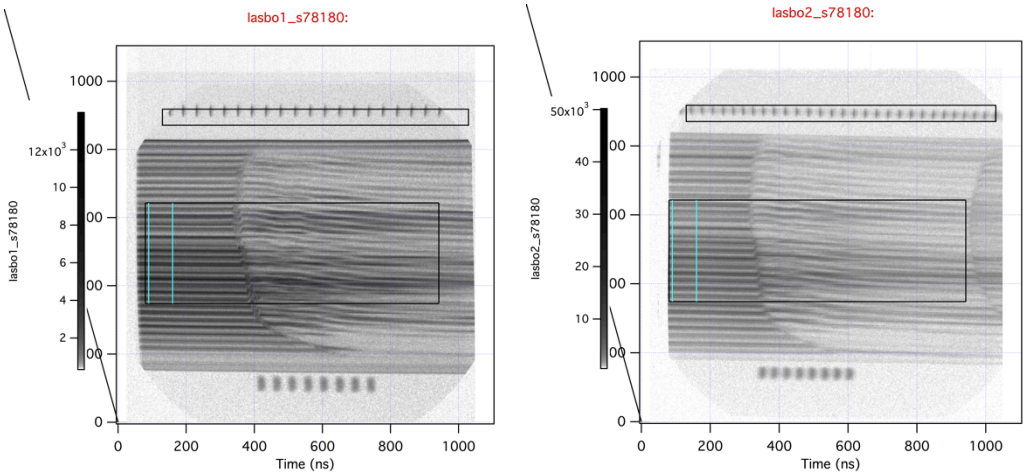

Figure 2. Raw VISAR data from ASBO 1 (left) and 2 (right).

4. Exploring the Earth's Lower Mantle (PI: D.E. Fratanduono)

with R.G. Kraus, D.K. Spaulding, D.G. Braun and P.M. Celliers (LLNL)

This campaign was motivated by a recent study[1] of $MgSiO_3$ using decaying shocks, which provided evidence for a liquid-liquid phase transition near 300 GPa. The primary objectives were to measure the adiabatic sound speed (C_s) and the Grüneisen coefficient (Γ) of single crystal $MgSiO_3$ along the principal Hugoniot from 200 GPa to pressures in excess of 800 GPa, including the proposed two-phase region, to further understand this transition. A secondary goal of these experiments was to accurately measure the principal Hugoniot of $MgSiO_3$ from 200 to 800 GPa by impedance matching with Quartz. Using the streaked optical pyrometer, we measured the temperature of $MgSiO_3$, which will provide a fully defined principal Hugoniot. These Hugoniot measurements near the proposed liquid-liquid phase transition will constrain the density discontinuity and overlap with separate gas gun experiments, as no measurements exist from 200 to 400 GPa. Measurements in this pressure range are of interest since recent density functional theory calculations show no presence of a liquid-liquid phase transition.[2] Two separate half days were conducted to study this transition in detail. The primary goals of the campaign were met in the first half-day. However, these experimental results drew into question the previous findings of Spaulding *et al.*[1] As a result, the second half-day of experiments were used to repeat the decaying shock experiment of Spaulding *et al.* However, these experiments were unable to reproduce the previous experimental findings.[1] The analysis is on-going in order to better understand the differences between these two experiments and proposed the liquid-liquid phase transition.

1. D. K. Spaulding, R. S. McWilliams, R. Jeanloz, J. H. Eggert, P. M. Celliers, D. G. Hicks, G. W. Collins, and R. F. Smith, Physical Review Letters **108**, 065701 (2012).
2. Burkhard Militzer, High Energy Density Physics **9**, 152 (2013).

5. Measurements of the Shear Strain of Vanadium Under Shock Compression (PI: C. Wehrenberg)

This was the first campaign to use in-situ diffraction to study shock compressed vanadium. Multiscale models of vanadium predict high strengths for high-rate loading due to the increased phonon drag resulting from the high temperatures associated with shock loading. This campaign used three UV beams to drive a zinc backlighter and the fourth UV beam to drive a shock into the vanadium foil. The goal of this campaign was to measure the shear strain in the shock compressed sample by measuring a difference in strain for different loading directions (corresponding to different diffraction lines). Seven shots were performed and high-quality data was recorded on several shots, with shock loading in the 0.5-1.7 Mbar range. Figure 1 shows a comparison between the static (undriven) data (Left) and data from a 0.5 Mbar shot (Right). The driven data has high-signal to noise and should allow a good measurement of in-situ shear strain.

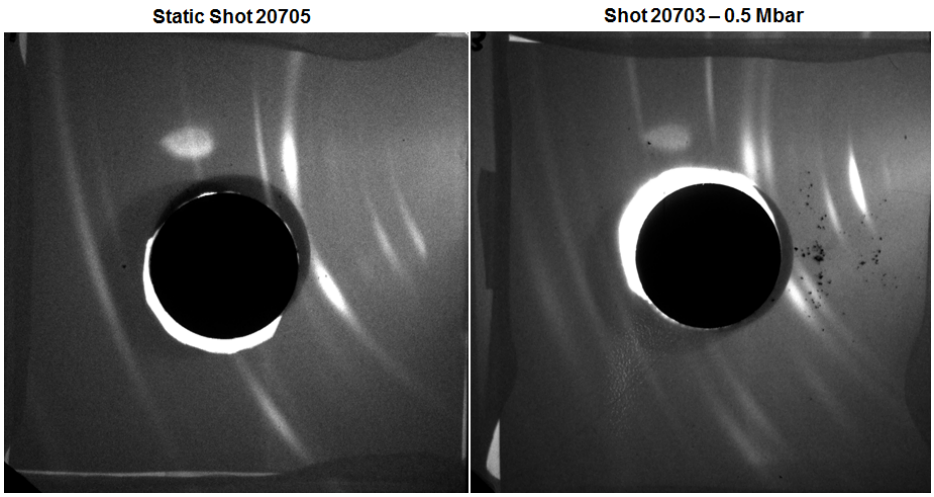

Figure 1: (Left) Diffraction from static vanadium. (Right) Diffraction from vanadium which has been shock compressed to 0.5 Mbar. Strain differences are revealed as changes in the pattern of X-ray diffraction features.

6. Phase separation of hydrocarbons at high pressures (PI: A. Pak)

with D. Kraus, T. Ma, T. Doeppner, J.A. Hawreliak, R. W. Falcone, T. Boehly, S. Hamel, D. O. Gericke, D. Chapman (LLNL)

We have begun to explore the predicted phase separation of hydrocarbons at densities of ~2 g/cc, temperatures of ~0.5-1 eV and pressures of ~1-2 Mbar. The relative phase between carbon and hydrogen atoms at such conditions is of interest as they are near to the predicted conditions within the interior of some carbon rich planets. The degree to which the atoms mix with each other impacts macroscopic quantities such as thermal and electrical conduction, which in turn affect the global planetary properties. In this work, spectrally resolved x-ray scattering was used to probe a hydrocarbon sample to infer the degree of phase separation. The experimental setup is shown in Figure 1 (a). Figure 1 (b) shows an example x-ray scattering spectrum. The compressed matter was probed at a central wave number of 3.8 $Å^{-1}$. The scattered spectrum is comprised of x-rays that scatter both elastically, at the incident x-ray energy, and inelastically, at lower x-ray energies. At the wave number at which the material was probed, density functional theory calculations predict that the amplitude of the elastically scattered x-rays will decrease as the amount of mixing increases between the hydrogen and carbon. These calculations indicate that the amount of mixing is sensitive to the temperature of the compressed material. Using the exquisite pulse shaping capabilities of the Omega EP laser, the hydrocarbon sample was compressed using two drive conditions. The first drive attempted to reach a 2X compression at relatively low temperatures with a 20 ns pulse shape that calculations indicate quasi adiabatically compresses the polystyrene (CH) target to about 2 g/cc and 0.5 eV. To increase the temperature and the amount of mixing, a second drive of 10 ns duration was designed to shock compress the CH target to a higher average temperature of about 1.5 eV at a similar compression. The EP laser was also used to create a zinc He-α x-ray line source at ~9 keV, which after scattering was spectrally and temporally resolved using the ZSPEC crystal spectrometer onto framing camera #5. As shown in Figure 1 (b), in contrast to theoretical predictions, the amplitude of the elastically scattered x-ray component increases as we attempt to increase the amount of mixing using the 10 ns drive. We are investigating whether geometrical and attenuation effects, in addition to timing jitter between the framing camera and the x-ray source, could explain the unexpected elastic scattering amplitude. Future work will focus on better characterizing the source to quantify the interplay between the elastic and inelastic scattering, better quantifying the drive material conditions for the two drive pulses with VISAR, and potentially making the measurements at lower scattering wave numbers, where the effect on the amplitude is expected to increase.

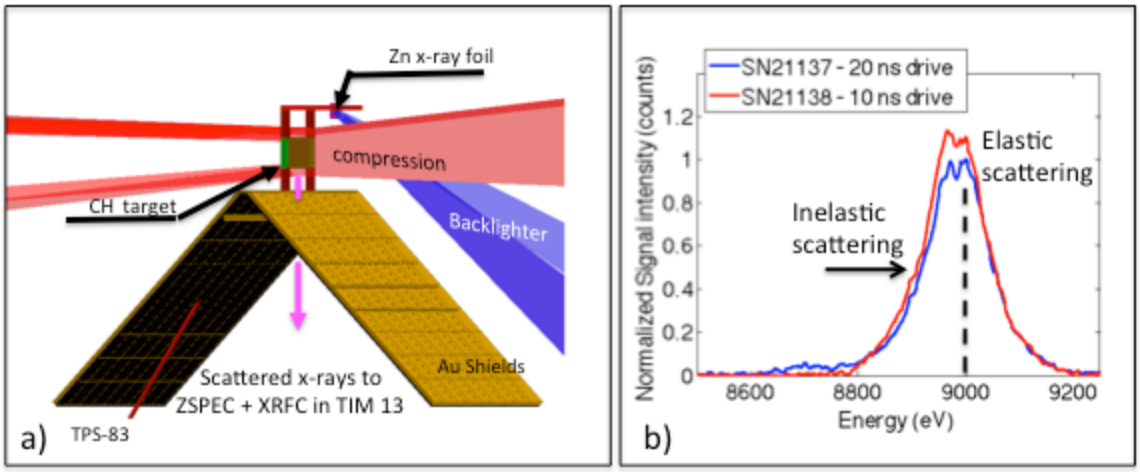

Figure 1 (a) Experimental setup. Two drive bundles compress the CH foil, while a probe bundle creates a burst of Zn He-a x-rays that scatter through the target. Scattered x-rays are collected via ZSPEC onto a framing camera detector in TIM 3. (b) The spectrally resolved scattered x-ray signal. Signal amplitude has been normalized using the signal from a time integrated Zinc Von Hamos spectrometer. The vertical dashed line indicates the central energy of the incident x-rays.

7. Eagle Pillar Formation on Omega-EP (PI: D.A. Martinez)

With C.M. Huntington, B. Villette, J.A. Emig, J. Kane, R.F. Heeter, A. Casner, and R. Mancini.

The LBS Eagle Pillar experiments investigated the early stages of formation of an astrophysical pillar. A copper 4-hohlraum array produces a 40ns x-ray source, which ablates a solid density CH target with a Cu nugget acting as a plasma source. Pillar formation was investigated using Omega-EP's 4ω shadowgraphy diagnostic, and the hohlraum drive was measured using CEA's TIM based mini DMX detector (Figure 1b). The shot day consisted of 7 shots varying the standoff distance of the target and looking at various times of the pillar evolution. The blowoff plasma from the hohlraum prevented very late time measurements of the pillar evolution, however excellent images were taken of the initial blow off of the foil (Figure 2). Figure 2a shows the initial shadowgraph with an initial standoff distance of 2mm. The distance was incrementally increased in order to avoid the blow off plasma from the hohlraum. Figure 2b shows the plasma blow off from the ablating Eagle target at 20ns with a 3mm standoff distance. Plasma from the hohlraum is seen interacting with the ablation from the Eagle target, creating shocks between the hohlraum and the target. For the 30ns image, the standoff distance was increased to 4mm; however, the increase in distance required an increase in x-ray drive, so two hohlraumes were driven simultaneously to double the x-ray flux via a 20ns rather than 40 ns drive. At this time the ablation plasma from the Eagle target is being pushed behind the target, and collecting in a converging conical flow behind the target, thus creating the initial pillar formation. As seen at the top of Figure 2c, this experiment provided the first evidence of pillar formation in the laboratory.

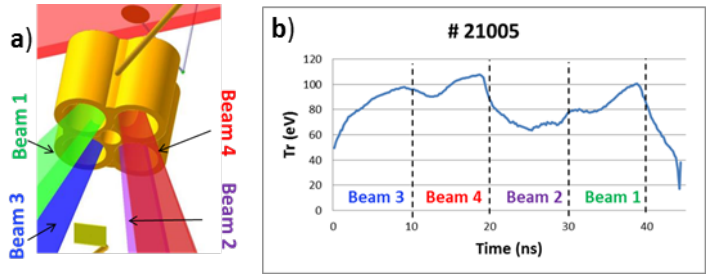

Figure 1: A) layout of the target showing the hohlraum array with four Omega EP UV beams and a photoionization target on the drive side, and the Eagle target behind the hohlraum. B) Results from mini DMX for a single shot with 40ns drive. (Signal level varies in part due to beam incident angle changes.)

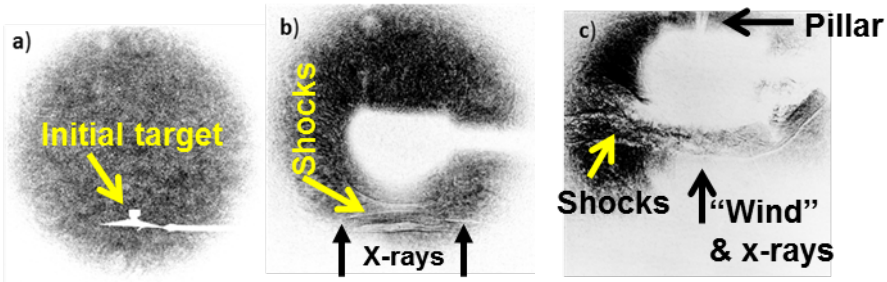

Figure 2: a) Initial target with a 2mm stand-off distance from hohlraum. b) Evolution at 20ns with 3mm stand-off distance. c) Evolution at 30ns with 4mm stand-off distance and increased drive. Evidence of initial pillar formation is seen behind the target.

8. Astrophysical Collisionless Shock Experiments with Lasers on EP (LBS PI: H.-S. Park; Shot PI: C.M. Huntington)

The Astrophysical Collisionless Shock Experiments with Lasers (ACSEL) campaign has been exploring the physics of interpenetrating plasma flows—flows that are effectively collisionless, but nonetheless interact strongly with each other, largely via self-generated magnetic fields. The flows are generated by laser ablation of opposing disks with up to 4.5 kJ of laser energy. Previous work [1, 2, and references therein] has measured the plasma properties of the resulting flow with Thomson scattering (TS), and proton radiography has revealed strong filamentation structures in the interaction region between the foils [3]. Beginning from this well-characterized platform, FY15 ACSEL experiments modified the system to better understand the dependencies and process of magnetic field generation.

Previous EM field imaging, using protons generated from D3He fusion in a capsule implosion, was performed perpendicular to the flows [ibid]. However, when the foils are tilted so that the protons probe a vector nearly along the flow direction, the small-scale filaments are measured closer to "end-on." Shown in Fig. 1, these measurements improve the understanding of the scale lengths present in the system, which are difficult to infer from a straight side-on measurement. Additionally, the spacing between the foils was also varied, to investigate the effects of plasma density and velocity distribution on the magnetic field generation. At present the proton radiography data is awaiting processing, but in conjunction with the high-quality TS data obtained for each shot, this new data will further the understanding of the hydrodynamic dependencies of the Weibel and related filamentation instabilities. Important insights for astrophysically-relevant collisionless plasma physics will be gained from these two FY15 OMEGA campaigns.

1. J. S. Ross, J. D. Moody, F. Fiuza, D. Ryutov, L. Divol, C. M. Huntington, and H.-S. Park. *Thomson scattering measurements from asymmetric interpenetrating plasma flows* a). Review of Scientific Instruments, 85(11), 2014.

2. J. S. Ross, H.-S. Park, R. Berger, L. Divol, N. L. Kugland, W. Rozmus, D. Ryutov, and S. H. Glenzer. *Collisionless coupling of ion and electron temperatures in counterstreaming plasma flows*. Phys. Rev. Lett., 110:145005, Apr 2013.

3. C. M. Huntington, F. Fiuza, J. S. Ross, et al. *Observation of magnetic field generation via the weibel instability in interpenetrating plasma flows*. Nat Phys, 11(2):173–176, 02 2015.

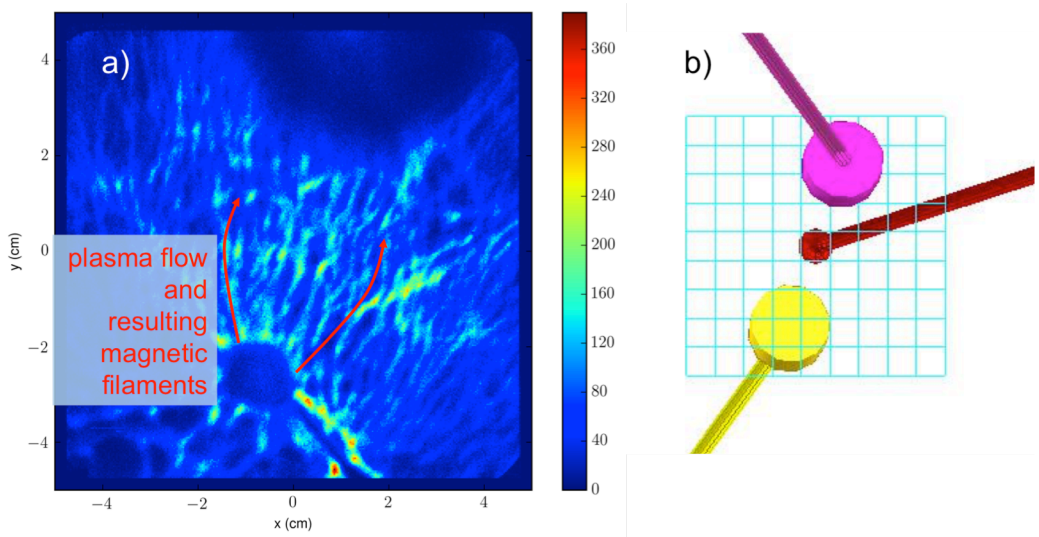

Figure 1: a) 14.3 MeV proton image showing filamentation along the flow direction, indicated by the red arrows; b) orientation of the two laser irreadiated targets (pink and yellow), with the D3He capsule (red) and approximate field indicated by the grid.

9. Exploring Pair Plasmas and Their Applications (PI: H. Chen)

In FY15, an LLNL/LLE team continued the project "Exploring pair plasmas and their applications" with 2 LBS shot days on OMEGA EP. The experiments used the short pulse beams to produce jets of electron-positron antimatter pairs. The experiments focused on measuring the pair yield and its dependence on the target material. The experiments successfully probed the basic physics processes involved in pair generation, and the data reveal discrepancies between experiments and theory. By alternating beams, a total of 28 shots were performed in 2 days.

The EP short pulse beams (~1 kJ in 10 ps) irradiated targets of 1 mm thick Au, Pb and U. In addition, targets of 1 mm thick Au with a gold nanowire front layer were also shot, to study the nano-wire effect on the yield of high energy photons and pairs. It was found that for the same laser energy, positron yields could be increased dramatically, depending on the target materials and the target surface. This finding is important to future experiments and applications using laser pair jets. Previous experiments used gold targets almost exclusively. These prior experiments showed that quasi-monoenergetic relativistic positron jets are formed during high-intensity irradiation of thick gold targets [1, 2], and that these jets can be strongly collimated [3] using the magnetized-inertial fusion electrical delivery system (MIFEDS) [4]. The external field produces a 40-fold increase in the peak positron and electron signal [3]. The positron yield was previously found to scale as the square of the laser energy [5], but the FY15 results revealed another dimension of scaling by varying the target materials. The favorable scaling would enable the laboratory study of relativistic pair plasmas that are important to understanding some of the most exotic and energetic systems in the universe [6].

[1] H. Chen et al., Phys. Rev. Lett. **102**, 105001 (2009).
[2] H. Chen et al., Phy. Rev. Lett. **105**, 015003 (2010).
[3] H. Chen et al., Phys. Plasmas **21**, 040703 (2014).
[4] O. Gotchev et al., Rev. Sci. Instrum. **80**, 043504 (2009).
[5] H. Chen et al., Phys. Rev. Lett. **114**, 215001 (2015).
[5] H. Chen et al., High Energy Density Physics, **7**, 225 (2011).